WELDING RESEARCH

SUPPLEMENT TO THE *WELDING JOURNAL*, DECEMBER 2023
Sponsored by the American Welding Society

A Novel Strategy for Realizing Reliable Welding of Aluminum-Steel

A resistance spot welding process of aluminum-steel dissimilar metals is proposed and its feasibility is evaluated

BY M. LI, Y. WANG, W. TAO, AND S. YANG

Abstract

This study proposed a novel welding strategy called active-expulsion-assisted resistance spot welding (RSW), which was used to address the limitations of RSW of aluminum to steel. The method primarily comprised an intentionally set expulsion stage and a locking stage. In the expulsion stage, a short-duration expulsion pulse with a relatively large welding current was applied to melt the aluminum and induce liquid aluminum expulsion. Then, in the locking stage, a welding current pulse was used to join the locking sheet and the steel workpiece. A combination of quenched and partitioned 1180 steel and AA6016 aluminum alloy with and without adhesive was used for welding. Experimental results showed that the expulsion pulse efficiently removed the aluminum alloy in the weld, creating the conditions for fundamentally avoiding the formation of brittle intermetallic compounds in the nugget during the subsequent welding stage. After the welding pulse, a strong joint was generated between the locking sheet and the steel, thus realizing a firm connection for the combination of welding and riveting between an aluminum alloy and steel substrate.

Keywords

- Aluminum
- Steel
- Active-Expulsion-Assisted Resistance Spot Welding
- Intermetallic Compounds
- Mechanical Property
- Adhesive Bonding

https://doi.org/10.29391/2023.102.022

Introduction

To reduce vehicle weight and energy consumption and improve the safety performance of vehicles, advanced high-strength steel, ultra-high-strength steel (UHSS), and aluminum alloy (Al) are increasingly being used in the automotive industry (Ref. 1). Connecting aluminum to steel is an inevitable issue to be solved for automotive manufacturing, and there are significant challenges in using traditional welding methods (Ref. 2). The low weldability of aluminum to steel can be mainly attributed to the following aspects. The poor mutual solubility of Al and Fe leads to the formation of a large volume fraction of brittle intermetallic compounds (IMCs), such as Fe_2Al_5 and $FeAl_3$, in the weld (Ref. 3), which deteriorates the mechanical properties of the joint when the thickness of the IMC layer grows greater than 1.5 μm (Ref. 4). The thermophysical properties of the two metals, such as the melting point, thermal conductivity, and expansion coefficient, differ considerably, which leads to a large residual stress, resulting in weld cracks (Ref. 5). The surface state of the workpiece, such as coating or oxide films, considerably influences the formation of weld discontinuities, such as porosities and cracks. Hu et al. (Ref. 6) determined that oxide films on the surfaces of aluminum alloys are incorporated into the weld, which lead to the formation of microcracks in the weld under the thermal stress induced by postpaint baking processes.

Various welding processes, such as solid-state welding, fusion welding, and brazing, have been used to produce high-quality aluminum-steel welds. To control or avoid the excessive formation of brittle IMCs in welds, welding parameters have been optimized, along with other metallurgic remedies such as the addition of, for example, Ge, Cr, Si, Zn, and Ti, inserting metal foils, prefabricating special coatings, and using designed welding wires (Ref. 7). However, it remains challenging to develop a universal welding process that can be used to join different combinations of aluminum and steel. Recently, some hybrid welding methods have been proposed to deal with these welding problems. Shah and Liu (Ref. 8) used ultrasonic-assisted resistance spot welding (RSW) to join aluminum and steel and found that the ultrasonic treatment

Table 1 — Chemical Compositions of the Materials (wt-%)

Material	Fe	Mn	Si	C	S	P	Cu	Mg	Zn	Cr	Ni	Al
Q&P980	Balanced	2.270	1.730	0.190	0.001	0.011						0.03
Q&P1180	Balanced	2.720	1.700	0.189	0.001	0.006	–	–	–	–	–	0.029
AA6016-T4	0.200	0.150	1.100	–	–	–	0.100	0.400	0.100	0.100	0.005	Balanced

Table 2 — Mechanical Properties of Q&P980, Q&P1180, and AA6016-T4

Material	Yield Strength (MPa)	Ultimate Tensile Strength (MPa)	Elongation (%)
Q&P980	743	1108	18
Q&P1180	1031	1235	15
AA6016-T4	127	240	29

Table 3 — Welding Parameters Corresponding to Different Experiments

Test	Clamping Force	Preheat Stage	Expulsion Stage	Welding Stage
AE-RSW	5 kN	5 kA-100 ms-1 pulse	16.4 kA-65 ms-3 pulse	13 kA-350 ms-1 pulse
AE-RSWB	5 kN	3.5 A-200 ms-1 pulse	16 kA-47 ms-3 pulse	13 kA-350 ms-1 pulse
RSW	5 kN	3 kA-150 ms-1 pulse	–	17 kA-160 ms-4 pulse

could break the oxide film, enhance the wettability of liquid aluminum, and change nucleation crystallization behavior. The magnetic field influenced the melt flow, temperature field, and element diffusion of the weld pool. Therefore, the formation of the IMC layer could be effectively controlled, and crack sensitivity in the weld was decreased when electromagnetic-assisted welding was used during aluminum-steel welding (Refs. 9, 10). These methods have improved weld formation and joint performance to some extent. However, the formation of IMCs in the weld under complex manufacturing techniques cannot be completely avoided.

Due to the poor weldability of aluminum to steel, the automotive industry strongly relies on adhesive bonding (AB) and mechanical joining processes for joining aluminum to steel. However, the adhesive layer during AB is influenced by service temperature and humidity, which changes the stress gradient in the adhesive layer and reduces the glass transition temperature and mechanical properties (Ref. 11). Furthermore, AB joints have poor cross tension and peel performance and are prone to large deformation, which can lead to debonding during high-temperature curing. Thus, the AB joint is seldom used in load-bearing components (Refs. 12, 13). However, a combination of AB and RSW is widely used in the automobile industry to join steel to steel and aluminum to aluminum. This combination can achieve better static strength, fatigue properties, and sealing performance of the joints (Ref. 14).

In the presence of an adhesive layer, however, it becomes more difficult for RSW to join aluminum to steel. According to Chen et al. (Ref. 15), there are several challenges in the use of the adhesive layer. First, the increased contact resistance at the interface results in higher heat resistance, which leads to the excessive growth of IMCs. Further, the deteriorated contact state causes molten aluminum to splash into the adhesive layer and damage it. Finally, inclusions and porosities are introduced in the weld because of the carbonization and vaporization of the residual adhesive layer at high temperatures.

Among mechanical joining processes, self-piercing riveting (SPR) is widely used to join dissimilar metals, such as aluminum and steel, because it does not involve a complex metallurgical reaction. However, when joining stackups with different gauges and thickness, SPR requires different rivets, dies, and rivet guns, which decreases manufacturing flexibility and increases manufacturing complexity (Ref. 16). Furthermore, it is challenging to join aluminum alloys to UHSS, which has an ultimate strength of > 700 MPa (Ref. 17). During SPR of aluminum and UHSS, the rivet tends to buckle and fracture and cracks form in the steel workpiece (Ref. 18).

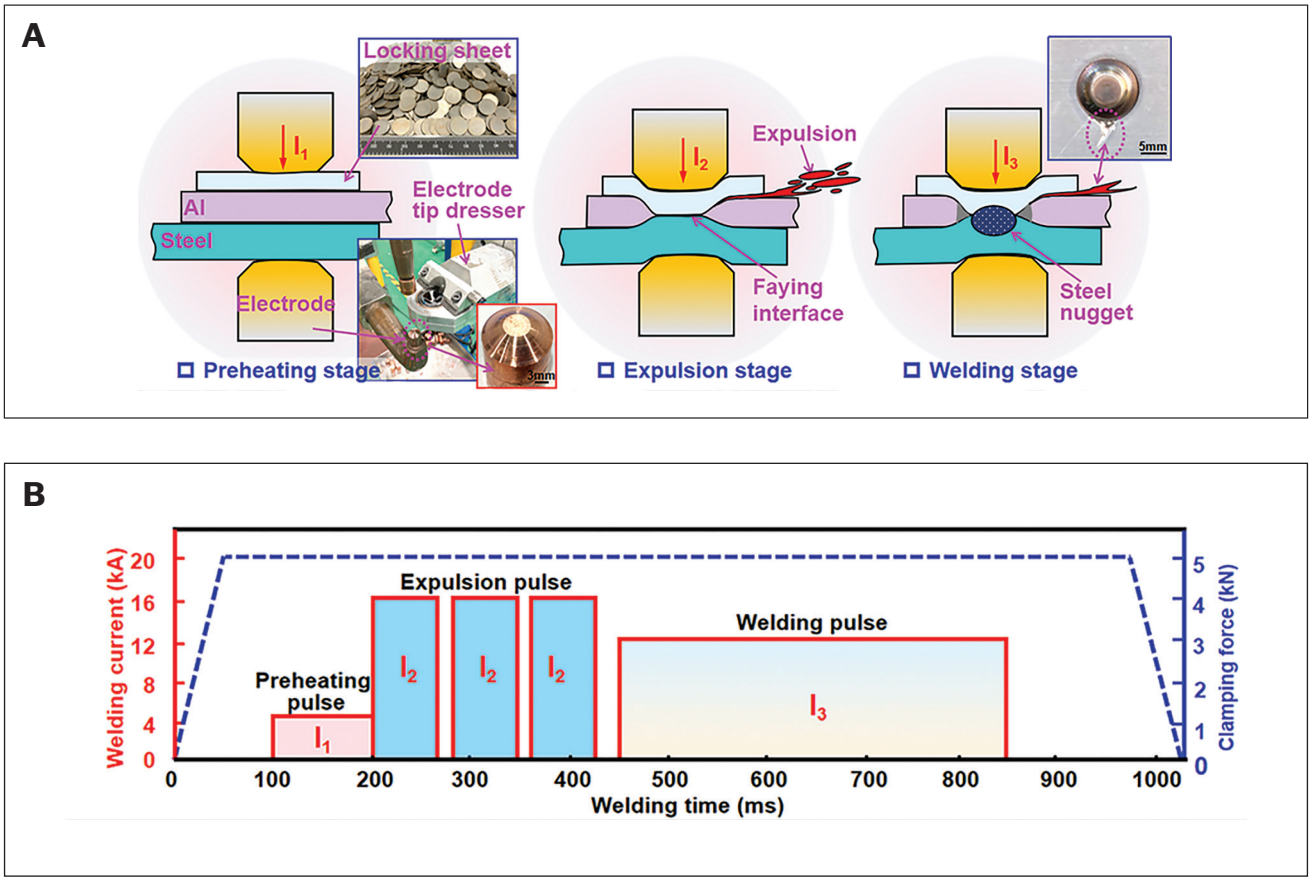

Fig. 1 — Schematic diagram and welding sequence of the AE-RSW process: A — The detailed AE-RSW welding process; B — the detailed welding schedule.

There is a need in the automotive industry to develop a reliable welding process that can help produce high-strength joints for dissimilar metals, such as aluminum steel. RSW is advantageous because of low cost, high efficiency, and a high degree of automation, and it is the mainstream joining technology in steel body-in-white (BIW) manufacturing (Ref. 19). During RSW of dissimilar metals, an excessively thick and uneven IMC layer and various weld defects are formed in the weld, which results in poor mechanical properties. Researchers have proposed several methods to address these challenges, such as optimizing the process parameters, redesigning electrode structures, and inserting intermediate layers (Refs. 20–22). However, these efforts can achieve very limited suppression of the formation of the brittle IMC layer in the weld. To avoid the effects of IMC formation, resistance element welding (REW) has been developed for achieving aluminum-steel joints. REW typically comprises two steps. First, a hole is predrilled in the aluminum sheet, and then, a steel rivet is inserted into this prehole, or an SPR process is used to insert a steel rivet in the aluminum sheet. Then, RSW is carried out on the steel rivet with the steel workpiece (Ref. 23). Compared with traditional RSW, REW results in more-reliable mechanical properties and, in theory, can join various combinations of dissimilar metals (Ref. 24). However, REW also has some limitations, such as long cycle time, complex rivet structures, and the need for concentric positioning between the welding electrode and the rivet during welding.

In this study, a novel welding process called active-expulsion-assisted RSW (AE-RSW) was developed. It was used to efficiently weld different dissimilar material combinations, such as Al/Fe, Mg/Fe, and Al/Ti. First, the welding parameters of AE-RSW were optimized and the microstructure characteristics of the joint with and without an adhesive layer were determined. Then, tensile shear tests were performed to evaluate the mechanical properties of the joint. Finally, the process of aluminum alloy expulsion during AE-RSW and the further work to be carried out in AE-RSW were discussed. The proposed method can effectively solve the longstanding problem of the formation of brittle IMCs and inconsistent weld quality and is a novel way for RSW of dissimilar materials.

Experimental Procedures

Materials and Welding Process

In this study, quenching-partitioning steel (Q&P1180) with a thickness of 1.2 mm (0.047 in.) and AA6016-T4 aluminum alloy with a thickness of 1.6 mm (0.062 in.) were used. A circular locking sheet was made using Q&P980 steel with a thickness of 1.0 mm (0.039 in.) and a diameter of 12.5 mm (0.492 in.). Their chemical compositions and mechanical properties are shown in Tables 1 and 2, respectively.

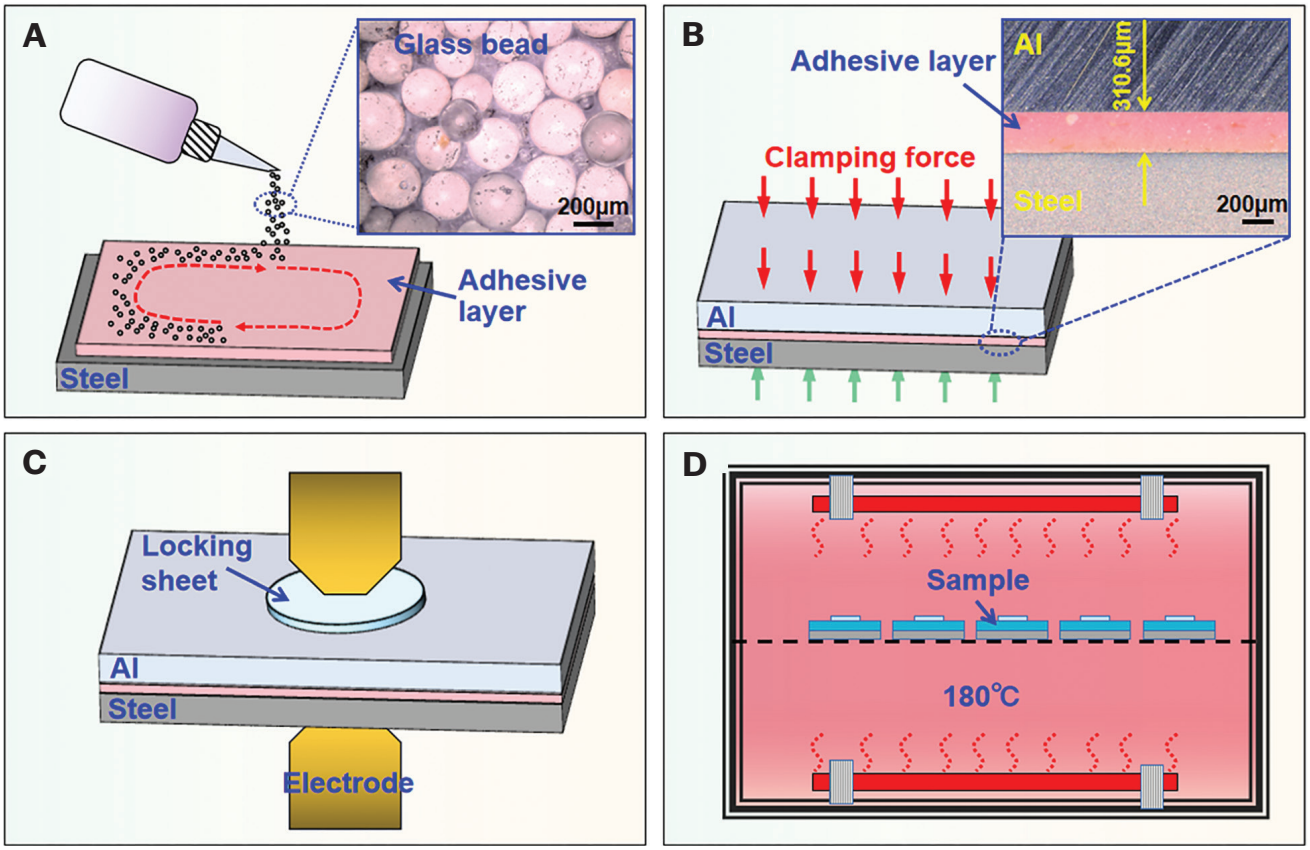

Fig. 2 — Schematic diagram of the AE-RSWB process: A — Glass beads laid on the adhesive layer; B — controlled thickness of the adhesive layer; C — AE-RSW; D — adhesive layer curing.

Figure 1A shows a schematic diagram of the AE-RSW process. There are two main differences between AE-RSW and traditional RSW. First, in AE-RSW, the locking sheet was directly welded on the steel substrate to produce a joint like a locking structure. This firmly locked the aluminum workpiece between the locking sheet and the steel workpiece. Second, an expulsion pulse was used before the welding pulse. The designed welding process comprised the following stages (Fig. 1B) (Ref. 25):

1) Preheating stage: A preheating pulse was applied to achieve better adherence between the workpieces, thus ensuring more-uniform and stable contact resistance between the metal sheets.

2) Expulsion stage: Several expulsion pulses with higher currents and shorter durations were applied immediately after the preheating stage. During this stage, the aluminum alloy in the welding area melted rapidly, and the molten metal was immediately ejected from the weld under the clamping force and its expansion pressure. As a result, an aluminum-free faying interface was produced between the locking sheet and the steel workpiece. In this work, the number of one to three different expulsion pulses was first optimized, and then three expulsion pulses were selected for the final joint preparation. The time interval of each expulsion pulse was set to 20 ms.

3) Welding stage: The cooling time was set as 30 ms before implementing the main welding process. The welding pulse with a smaller current and a long time melted the faying interface to form a steel weld nugget, which, in turn, firmly locked the aluminum alloy.

In this work, experiments were carried out using a medium-frequency direct-current RSW system, and Cr-Zr-Cu dome-shaped electrodes were used during welding. Before welding, all welding electrodes were refurbished using a commercial dresser (Fig. 1A). Electrode tip size considerably influences weld deformation, current density distribution, and resistance heat transfer. To facilitate the concave deformation of the locking sheet and steel workpiece during the expulsion stage in AE-RSW, a dome-shaped electrode with a tip diameter of 6 mm (0.236 in.) and spherical radius of 50 mm (1.968 in.) was used. In traditional RSW of Al-steel, a dome-shaped electrode with a tip diameter of 10 mm (0.393 in.) and spherical radius of 100 mm (3.937 in.) is typically used to avoid rapid electrode degradation. In RSW, four welding pulses were applied to the joint, which allowed the nugget to undergo repeated melting and solidification and restrained the formation of weld defects and excessive growth of IMCs. The detailed welding parameters are given in Table 3.

Active-Expulsion-Assisted Resistance Spot Welding-Bonding

Figure 2 shows the detailed schematic diagram of the AE-RSW-bonding (AE-RSWB). First, a Betamate™ 1840C

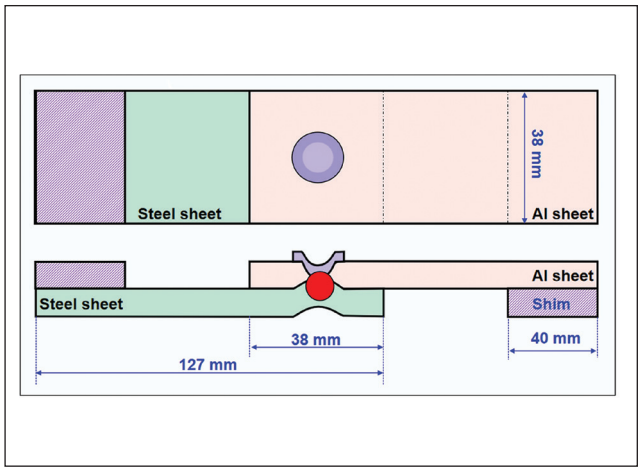

Fig. 3 — Sample specification for tensile shear tests.

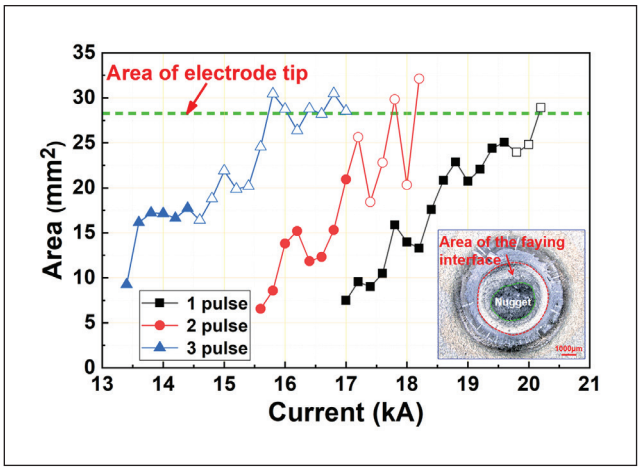

Fig. 4 — Area change of the faying interface varying with expulsion pulse amounts and current values (hollow symbols correspond to the formation of a steel nugget in the joint).

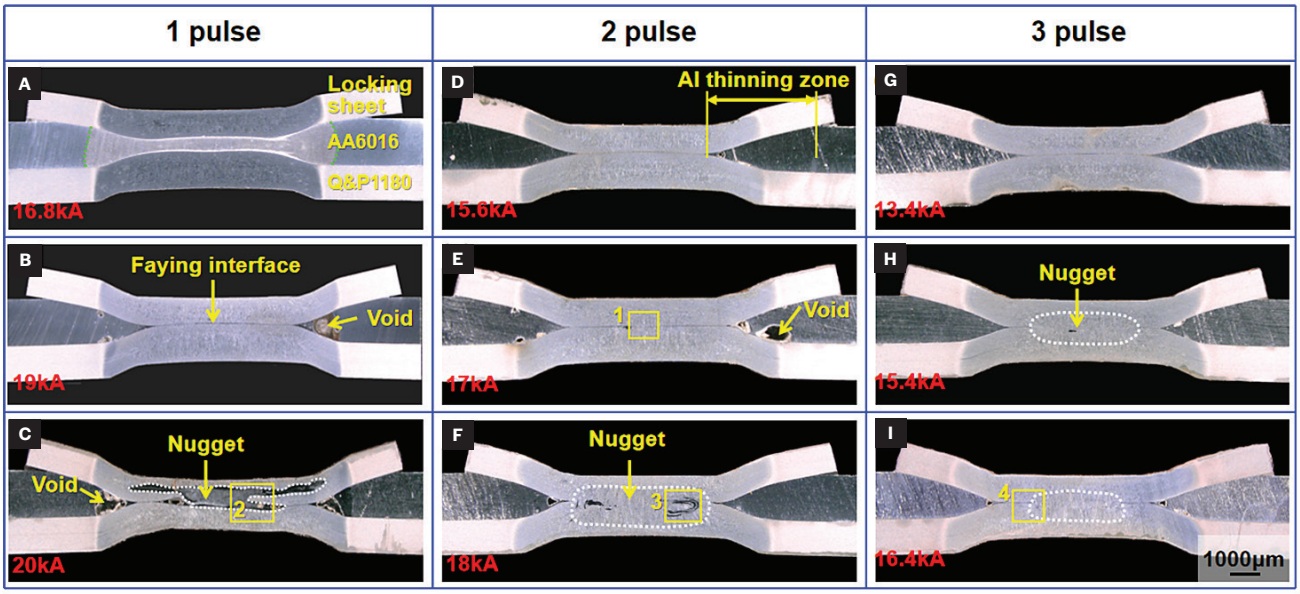

Fig. 5 — Cross section of the joints obtained using different expulsion pulses and current values: A–C — One expulsion pulse; D–F — two expulsion pulses; G–I — three expulsion pulses.

adhesive layer was applied to the surface of the steel workpiece using a hand-held injection gun, and then a commercial glass bead with a diameter of 300 μm was laid around the periphery of the adhesive layer to control its final thickness (Fig. 2A). After the aluminum plate was applied to cover the adhesive layer, a binder clip was used to apply pressure on the stacked workpiece and allowed to remain for > 40 min to discharge the excess adhesive and obtain a uniform thickness of the adhesive layer (Fig. 2B). Subsequently, the joints were welded according to the welding schedule of the AE-RSWB process (Fig. 2C). The detailed AE-RSWB parameters are shown in Table 3. After welding, the samples were placed in an oven to cure the adhesive layer at 180°C (356°F) for 30 min.

Metallographic and Mechanical Properties Testing

The macroscopic and microscopic structure of the cross section of the joint was observed using an ultra-deep metallurgical microscope (OM, Keyence VHX-6000) after etching with 4% Nital and Keller's reagent. The microstructure and elemental distribution were determined by characterizing using field emission scanning electron microscopy (SEM5000) integrated with energy dispersive spectroscopy (EDS) and electron backscattered diffraction. The hardness distribution of the welds was determined using a microhardness tester (Vickers 402 MVD). The test loads for the steel and aluminum sides were 200 and 100 gf (g

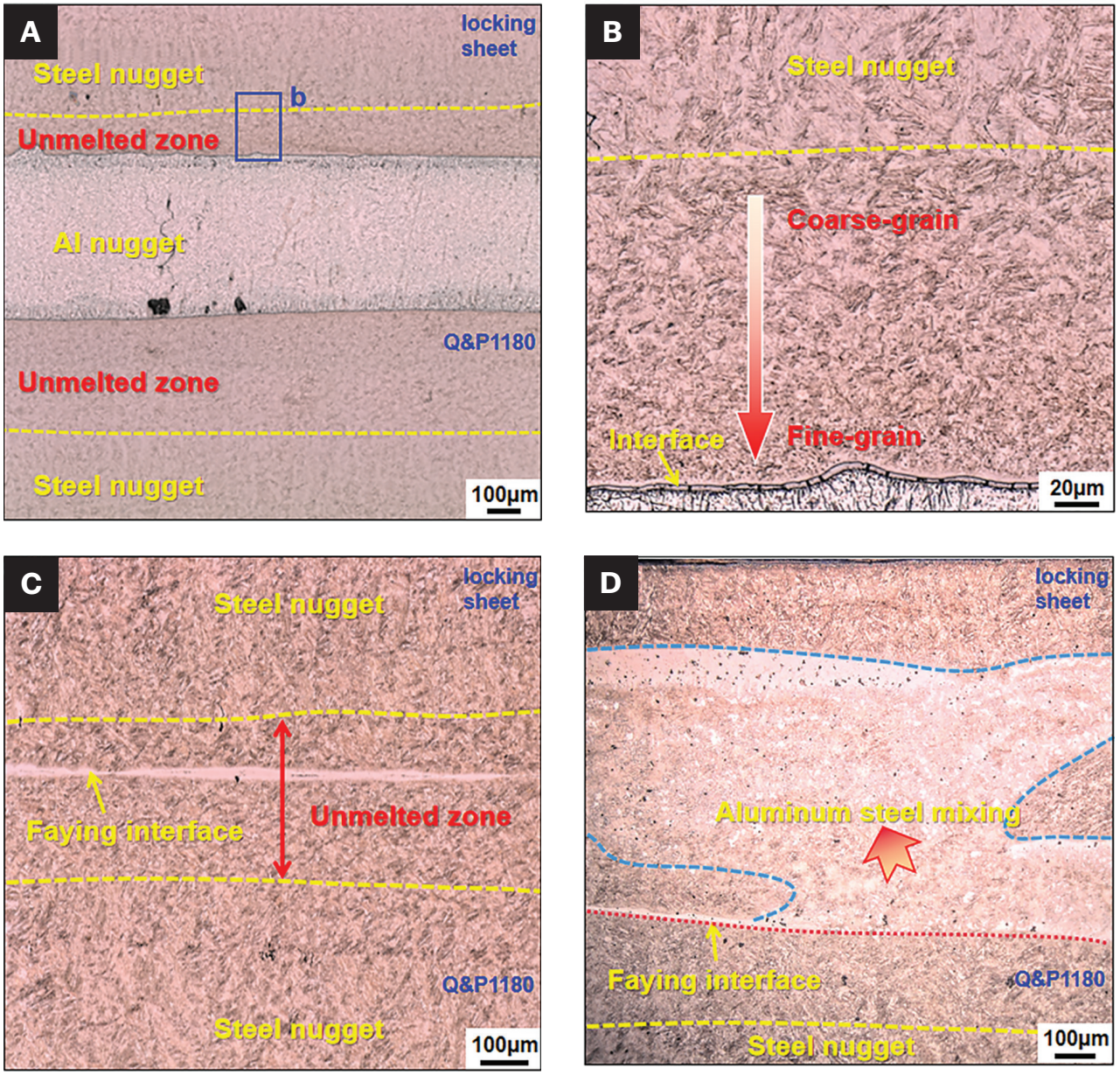

Fig. 6 — Microstructure of the weld with one expulsion pulse: A — Weld center of Fig. 5A; B — enlarged view; C and D — weld centers of Figs. 5B and C, respectively.

represents the acceleration of gravity and f represents the abbreviation of force), respectively. Tensile shear tests of the AE-RSW and RSW joints were carried out using a universal testing machine (UTM5015) at crosshead speeds of 3 and 1 mm/min (0.118 and 0.039 in./min), respectively, to evaluate their static mechanical properties. The specifications of the tensile shear sample are shown in Fig. 3. VIC-3D digital image correlation (DIC) was used to capture the strain distribution of the AE-RSW joint in real time during the tensile shear test. Energy absorption of the joint was typically accompanied by peak load to describe joint strength, which is the area covered by the load-displacement curve before reaching the peak load (Ref. 26).

Results

Effects of Different Expulsion Pulses on Weld Nuggets without Adhesive

To reveal the effect of different numbers of expulsion pulses and current values on the removal of aluminum in the joint, the area of the faying interface was measured after different expulsion pulses, and the results are shown in Fig. 4. The faying interface in which the locking sheet was in direct contact with the steel workpiece was easily obtained by applying single or multiple expulsion pulses (Fig. 5). The faying interface area increased, but it did not exhibit a linear relationship with the increased current due to the inconsistent

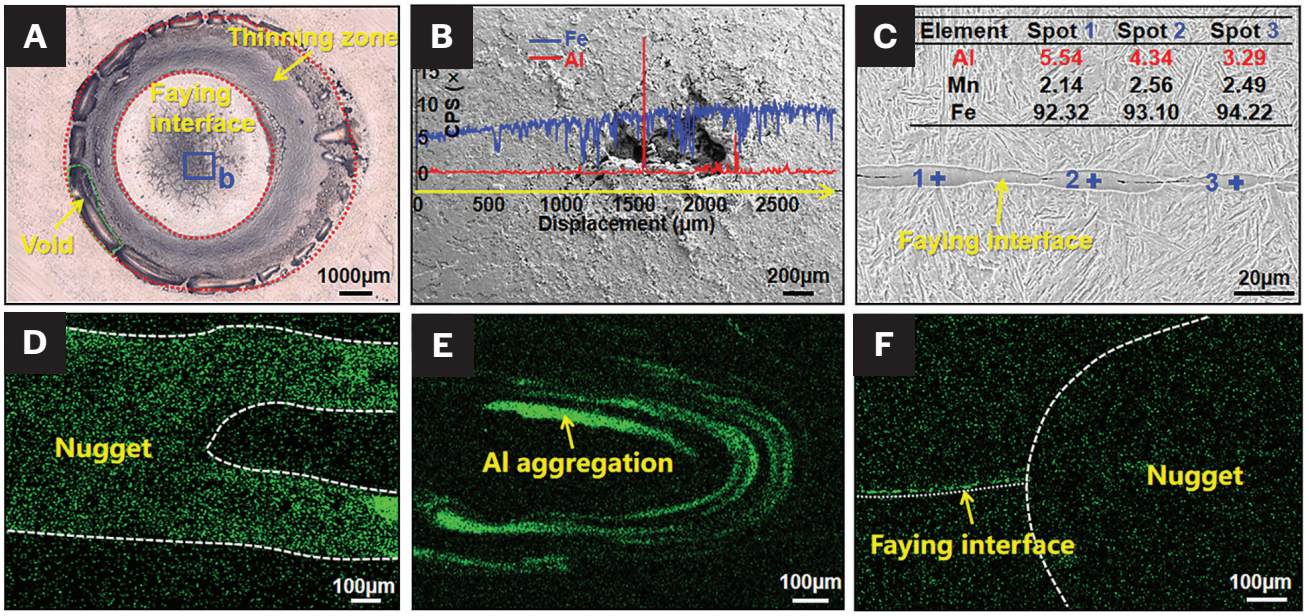

Fig. 7 — Microstructure and element distribution of the joint after the expulsion stage: A — Interface morphology with two expulsion pulses of 17 kA; B — line distribution of elements; C — chemical compositions of the faying interface in box 1 of Fig. 5E (given in weight percentage); D–F — Al element mapping of boxes 2–4 in Fig. 5.

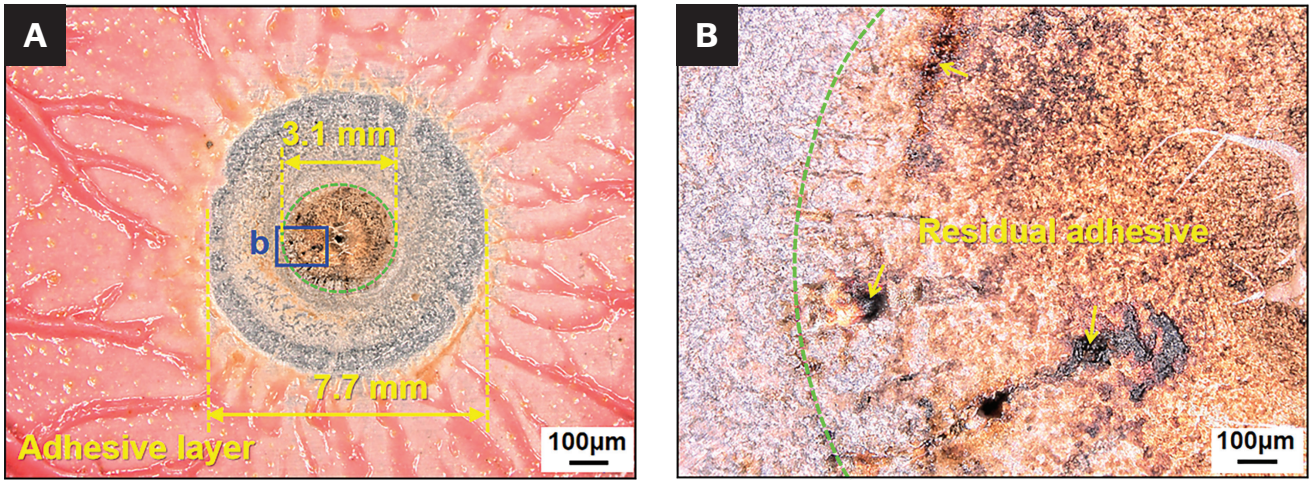

Fig. 8 — Influence of the preheating pulse on the joint: A — Overall view of the adhesive layer; B — enlarged view of the joint center.

overall initial contact resistance, which resulted in varied heat generation and level of expulsion. These were attributed to variations such as part surface finish and its fitup and electrode conditions, which could not be strictly controlled during RSW. When the current increased to a certain value, the area of the faying interface was close to the area of the electrode tip. In addition, the formation of the faying interface under the action of a single expulsion pulse required a larger current. As the number of expulsion pulses increased, a smaller current value could induce the expulsion process to form the faying interface, and the steel weld nuggets were more likely to form.

Figure 5 shows the cross-sectional structure of the joints obtained using different expulsion pulses and current values. A deep electrode imprint was produced on the surface of the weld due to the instantaneous loss of molten aluminum alloy in the middle layer. When the resistance heat generated by the expulsion pulse was too small to generate an expulsion phenomenon or when the expulsion was insufficient, the aluminum alloy was not completely pushed out from the joint area to form a faying interface between the locking sheet and the steel sheet, as shown in Fig. 5A. Once the resistance heat reached a specific threshold, a perfect faying interface without a thick aluminum layer (> 100 μm) was obtained (Figs. 5B and E) whether single or multiple expulsion pulses were applied. As shown in Figs. 5F, H, and I, a common nugget between the locking sheet and the steel workpiece was also formed in the joint. Its formation was attributed to a larger expulsion pulse, which removed aluminum and also promoted the melting of

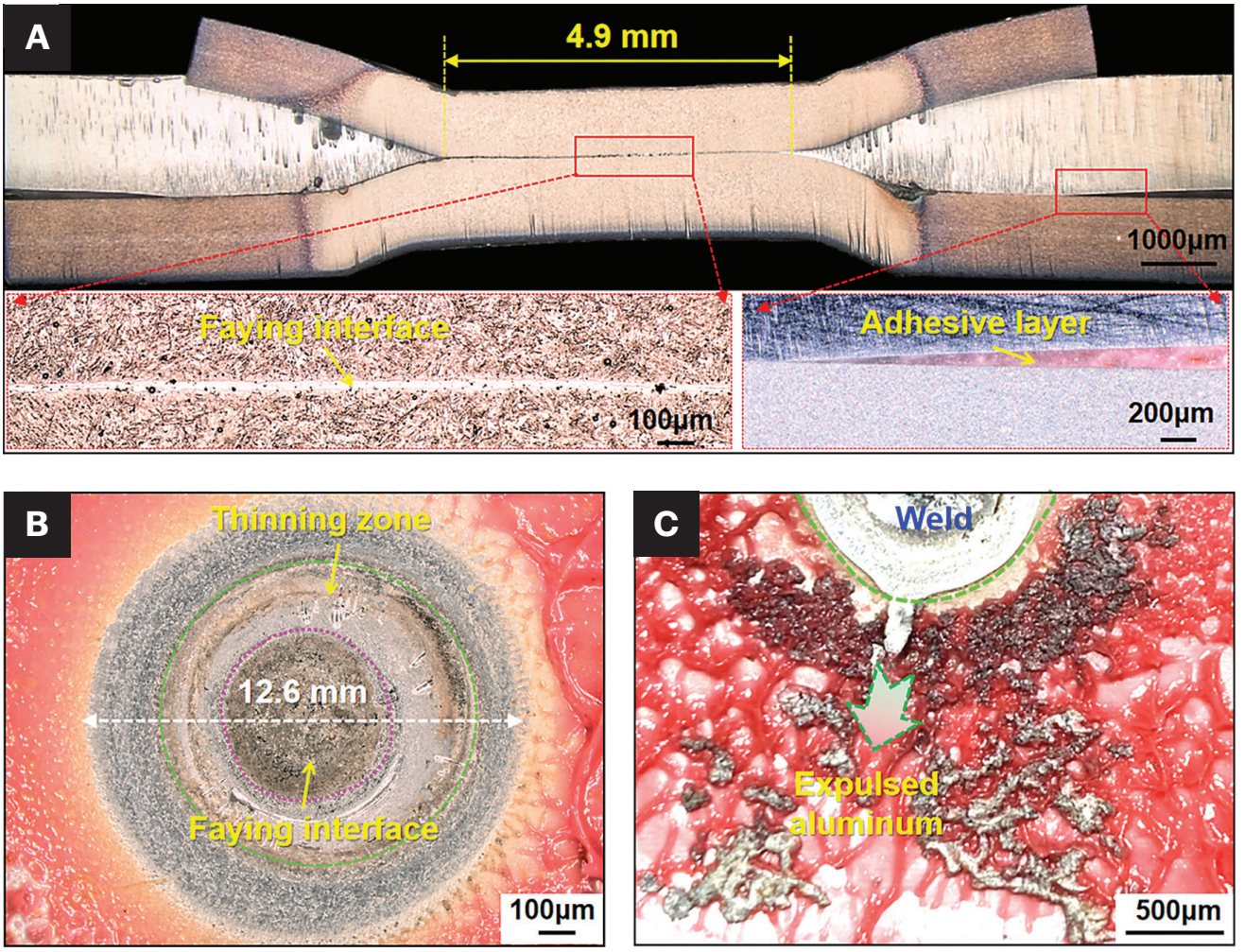

Fig. 9 — Joint after three expulsion pulses: A — Cross-sectional structure; B — adhesive layer on the aluminum-steel interface; C — expulsion metal in the adhesive layer.

the steel. The aluminum thinning zone had some voids because of the excessive loss of aluminum, and these were distributed circumferentially around the welding spot (Figs. 5E and 7A). In comparison, the joint with three expulsion pulses produced the least number of voids because of its smaller current value, which decreased the magnitude of the drastic increase in resistance heat and the area where the aluminum alloy was melted.

Figure 6 shows the microstructure at the central part of the weld using one expulsion pulse. In case of incomplete expulsion, an obvious boundary was observed in the joint (Fig. 6A). It divided the locking sheet and the aluminum and steel workpieces. The respective steel weld nuggets were formed inside the locking sheet and steel workpiece. There was an unmelted zone between the steel nugget and the aluminum alloy in the intermediate layer. In the unmelted zone (Fig. 6B), the martensite grains changed from coarse to fine closer to the aluminum-steel interface. This was attributed to the steep temperature gradient formed in this zone because of the considerably different thermophysical properties of steel and aluminum. In the case of joints where the aluminum alloy was completely removed, unmelted zones were still observed on both sides of the faying interface (Fig. 6C). However, when the current value of the expulsion pulse increased to 20 kA, a large amount of liquid aluminum mixed with the liquid of the steel nugget in the locking sheet (Fig. 6D).

Figures 7A–C show the element distribution of the faying interface after two expulsion pulses of 17 kA. An approximately circular faying interface was formed in the joint, and the EDS line scanning results of Al (red line) showed that there was only a trace amount of aluminum residue at the interface (Figs. 7A and B). The EDS spot scanning results of the cross section further showed that the average Al content at the faying interface was 4.39 wt-% (Fig. 7C). Thus, the molten aluminum was efficiently and remarkably removed by the expulsion pulse. When two expulsion pulses with large current values (18 kA) were applied, a considerable amount of aluminum was accumulated in the nugget formed (Fig. 7E). It was not as serious as the nugget formed using one expulsion pulse of 20 kA (Fig. 7D). Furthermore, aluminum did not accumulate in the nugget with three expulsion pulses (16.4 kA) (Fig. 7F). Based on the above results, aluminum removal was most efficient when three expulsion pulses were applied. Three expulsion pulses required less current, which was beneficial for avoiding the formation of voids in the aluminum thinning zone. Therefore,

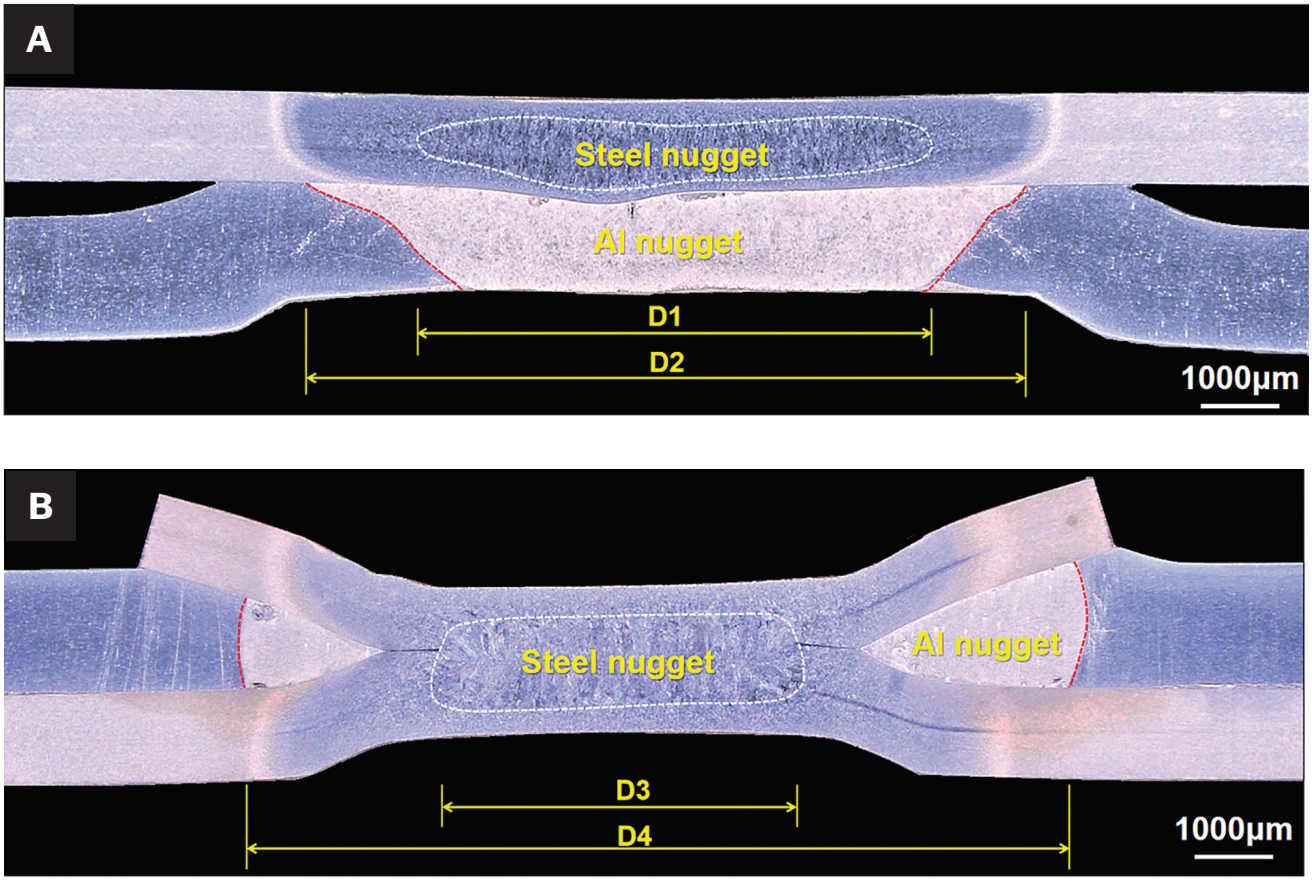

Fig. 10 — Cross-section views of the joint after the welding stage: A — RSW; B — AE-RSW.

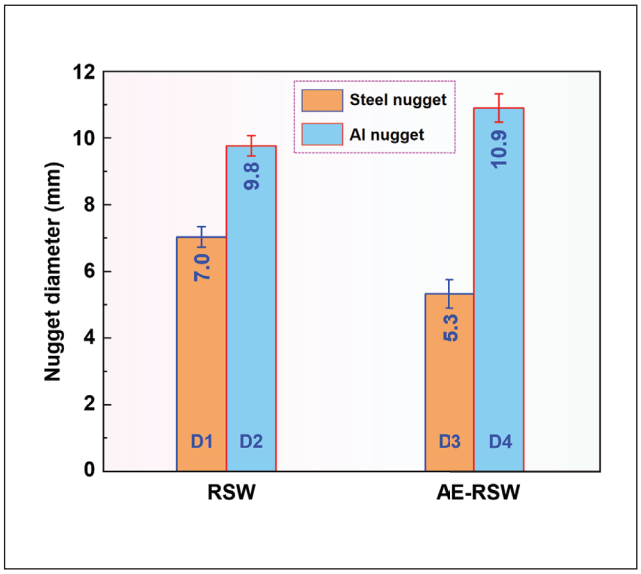

Fig. 11 — Nugget diameter.

three expulsion pulses were used to remove the aluminum alloy during the expulsion stage for subsequent sample preparation.

Effect of Expulsion Pulse on the Joint with Adhesive Layer

Figure 8 shows the distribution of the adhesive layer in the joint after the preheating stage. Heating the adhesive layer increased its fluidity, which was conducive to its discharge from the weld, thus allowing the workpiece to fit more closely. As shown in Fig. 8A, an area with a diameter of 7.7 mm (0.303 in.) was free from the adhesive layer, which was slightly greater than the diameter of the electrode tip. However, due to the local melting of the aluminum workpiece in the center of the weld, a small amount of the adhesive layer was carbonized at high temperature and remained in the joint (Fig. 8B).

Figure 9 shows the joint after the expulsion pulse action. The aluminum alloy in the weld was also completely expelled from the joint by the induced expulsion process, thereby forming a faying interface without residual aluminum alloy and adhesive layer (Fig. 9A). During the expulsion stage, the squeezing effect of the electrode was extended through the locking sheet to the whole area of the aluminum sheet that was in direct contact with the locking sheet. This caused the adhesive layer to be fully squeezed beyond the area radiated by the diameter of the locking sheet (12.6 mm [0.496 in.]) (Fig. 9B). Notably, expulsion in the joint with the adhesive layer was not always discharged from the interface between the locking sheet and aluminum. In some cases, molten alu-

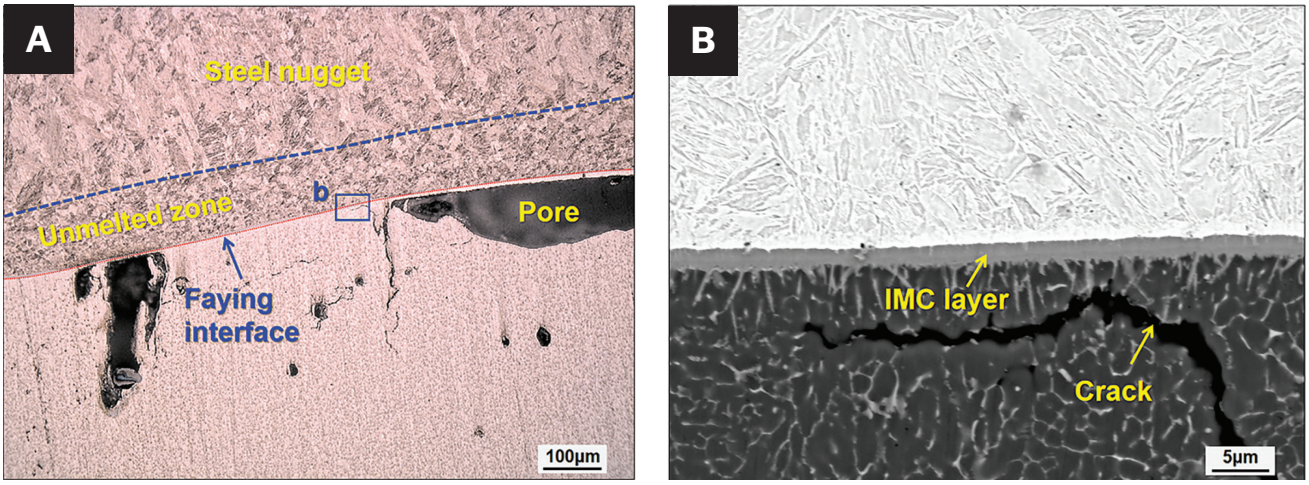

Fig. 12 — Weld center of Fig. 10A: A — Microstructure of the interface; B — IMC layer.

minum entered the adhesive layer under the action of the expulsion pulse, as shown in Fig. 9C, which decreased the AB area and its bonding ability.

Microstructure Characterization of Joints

Figure 10 shows the cross-sectional structures of the joints. For the traditional Al-steel RSW joint, an isolated steel nugget was formed inside the steel sheet, and the aluminum nugget was attached to the faying interface, achieving Al-steel metallurgical bonding (Fig. 10A). As shown in Fig. 11, the diameters of the steel and aluminum nuggets were 7.0 and 9.8 mm (0.275 and 0.385 in.), respectively. In traditional Al-steel RSW, the aluminum nugget can easily overgrow from the faying interface to the surface of the joint, which deteriorates the surface quality and accelerates the rapid degradation of the welding electrode. The aluminum workpiece around the joint was deformed severely, which produced a large gap between aluminum and steel (Fig. 10A).

As shown in Fig. 12A, there were some cracks and pores in the aluminum nugget of the RSW joint. Cracks were formed because of high residual stress, which was attributed to the rapid solidification of the Al nugget (Ref. 8). These pores were formed because of factors such as volume shrinkage during solidification, evaporation of light elements (e.g., Mg and Zn), and the evolution of hydrogen during solidification from water trapped in the surface oxides (Refs. 22, 26). Due to the high thermal conductivity of the aluminum alloy, the temperature decreased rapidly from the steel side to the aluminum side, which inhibited the expansion of the steel nugget to the Al-steel interface, thus forming an unmelted zone between the steel nugget and the faying interface (Fig. 12A). Aluminum nuggets formed metallurgical bonds by interdiffusion of elements after wetting to a solid steel surface. Therefore, a continuous IMC layer with a thickness of ~ 2 μm was formed on the faying interface, as shown in Fig. 12B. Several studies have confirmed that this layer comprised a Fe_2Al_5 sublayer adjacent to the steel side and a $FeAl_3$ sublayer adjacent to the aluminum side (Refs. 4, 6).

For the AE-RSW joint, the locking sheet and the steel workpiece were welded together through a steel nugget with a diameter of 5.3 mm (0.208 in.), as shown in Fig. 10B. There were no obvious aluminum alloy residues and macroscopic pores and cracks in the steel nugget. The diameter of the aluminum nugget surrounding the peripheral area of the joint was 10.9 mm (0.429 in.) (Fig. 11). Finally, the aluminum sheet was firmly locked into an X-shaped joint formed by the locking sheet and the steel workpiece. Compared with the RSW joint, no large gap was found between the contact surfaces of the aluminum and steel workpieces, indicating that the AE-RSW process did not cause severe warping of the workpiece around the joint despite significant imprinting of the electrodes (Fig. 10B).

Figure 13 shows the hardness mapping and local microstructure of the AE-RSW joint. The orange zone on the cross section of the joint was the weld nugget and heat-affected zone (HAZ), and its hardness (~ 500 Hv) was much higher than that of the base metal (Q&P980: ~ 300 Hv; Q&P1180: ~ 375 Hv) (Fig. 13A). Wang et al. (Ref. 27) pointed out that in addition to 80.5% martensite, there was 7.8% soft ferrite and 11.7% austenite in the Q&P1180 base metal (volume fraction) (Fig. 13E). However, the molten steel in the nugget was transformed into austenite and then into full martensite during rapid cooling (more than 2000°C/s [3632°F/s) (Fig. 13B), which increased the hardness of the nugget (Ref. 28). Furthermore, aluminum is a strong stabilizer for ferrite, and it promotes the formation of ferrite with low hardness when mixed with the weld nugget (Ref. 29). The nugget with all martensite phases further demonstrated that the trace amount of aluminum remaining on the faying interface after expulsion pulse did not influence the weld microstructure.

Several low-hardness points in the center of the weld nugget were formed by the shrinkage voids caused by rapid solidification and shrinkage of the nugget during cooling (Fig. 13B) (Ref. 30). The temperature of the HAZ near the nugget was higher than A_{c3}, which was conducive to the complete austenite transformation and the growth of austenite grains in this area. During the rapid cooling process, the austenite transformed into high-hardness coarse martensite (Fig. 13C). In the orange-to-green transition zone (intercritical HAZ), the temperature gradually decreased to near A_{c1}, resulting in incomplete austenitization; as a result, some ferrite was retained, leading to decreased hardness (Fig. 13D) (Ref. 31).

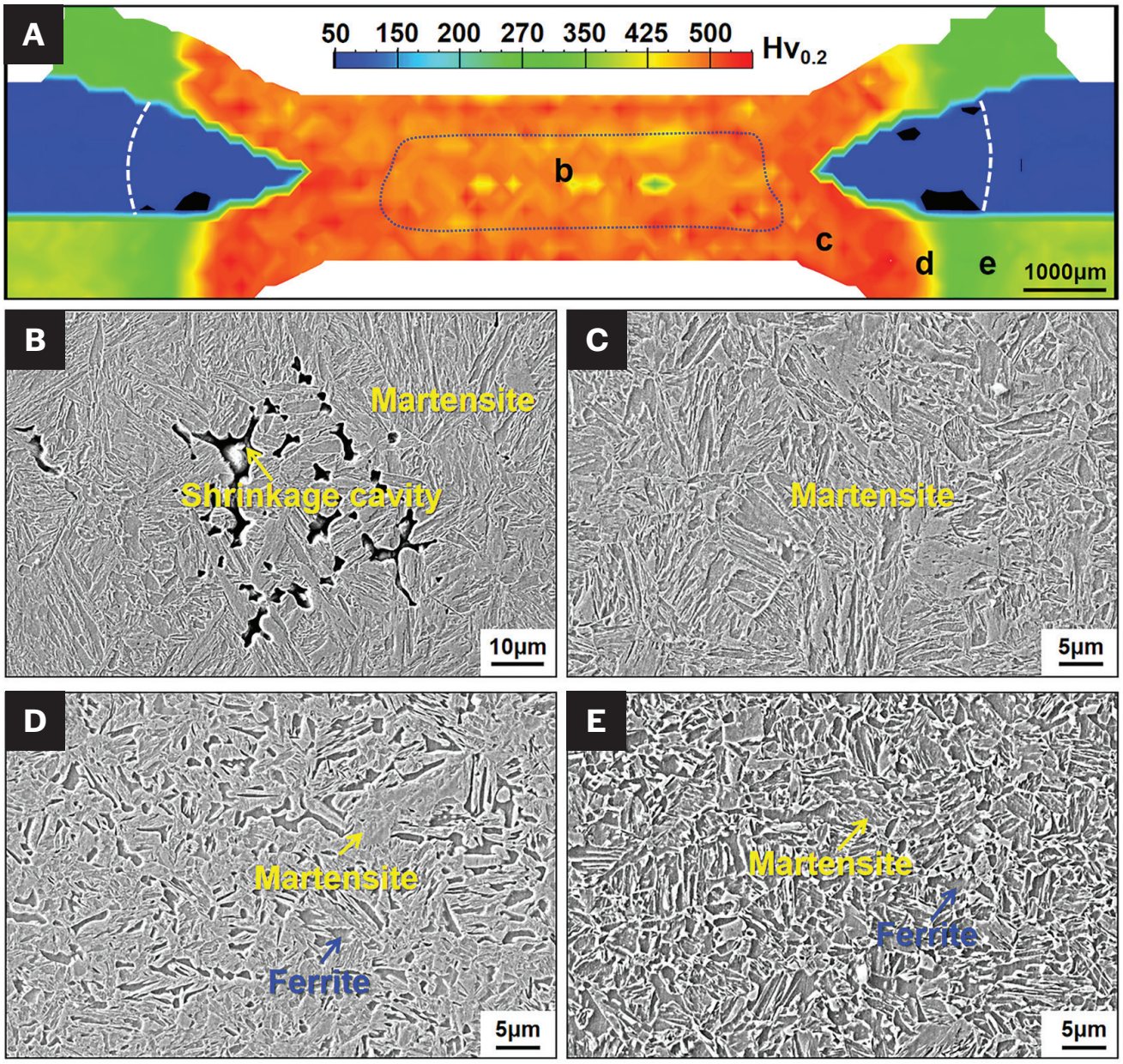

Fig. 13 — Hardness and microstructure of the AE-RSW joint: A — Hardness mapping; B — nugget; C — coarse grain HAZ; D — intercritical HAZ; E — base metal.

The IMC layer was also formed at the interface between the aluminum nugget and the steel because of the mutual diffusion of aluminum and iron, as shown in Figs. 14A and C. The microhardness distribution from the aluminum base metal to the equiaxed grains region in the aluminum thinning zone is shown in Fig. 14B. The hardness in the melting area was slightly higher than that of the base metal. Because of the high thermal conductivity of the aluminum alloy, a large amount of resistance heat in the aluminum nugget was dissipated by the aluminum workpiece, which promoted the growth of columnar grains from the weld interface toward the center of the weld (Fig. 14E). The heat dissipation then decelerated near the notch root, which moderated the temperature gradient and promoted the coarsening of equiaxed grains (Fig. 14F). Kernel average misorientation (KAM) was used to measure the concentration degree of geometrically necessary dislocation density and local strain distribution (Ref. 32). The KAM in the nugget was slightly larger than that of the base metal, and the KAM in the equiaxed grain zone was the largest. This was because the locking sheet and the steel workpiece had a more significant extrusion effect on the tip of the aluminum nugget during the welding process. This explains why the hardness of the nugget was slightly higher than that of the base metal.

The cross-sectional structure of the AE-RSWB joint is shown in Fig. 15A. The steel nugget was also successfully formed in the joint. There were no large-scale voids caused by the residual adhesive layer and no traces of large amounts of residual aluminum residues. The nugget structure was also full mar-

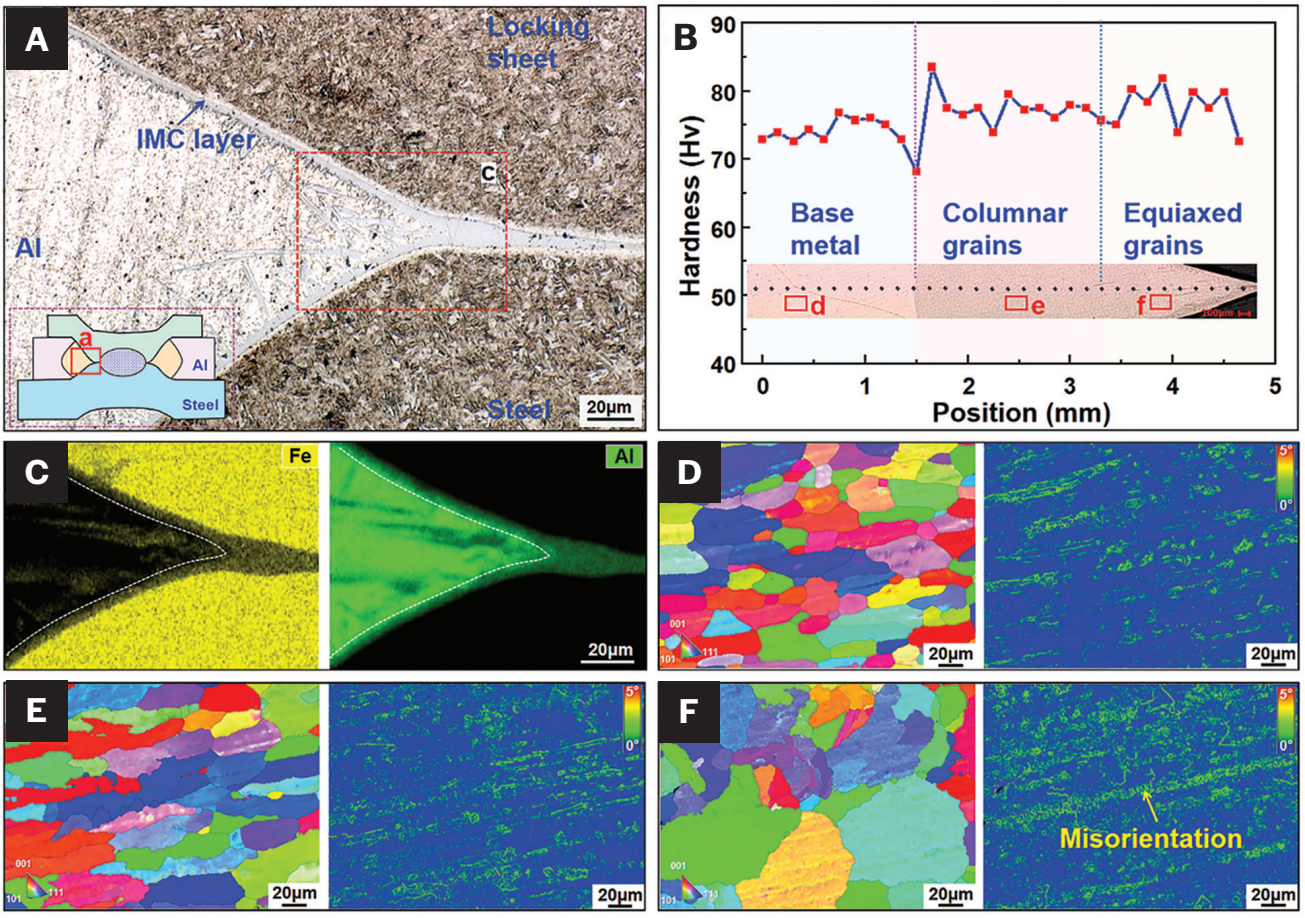

Fig. 14 — Microstructure and hardness of the aluminum nugget in the AE-RSW joint: A — Interface; B — hardness; C — EDS mapping analysis; D–F — inverse pole figures and KAMs of base metal, columnar grain zone, and equiaxed grain zone, respectively.

tensite. The IMC layer was formed at the interface between the aluminum nugget and steel substrate (Fig. 15B), and only a small amount of residual adhesive layer was mixed into the aluminum nugget (Fig. 15C). The adhesive-free area in the joint further expanded to 14.3 mm (0.562 in.) because of the further extrusion of the joint by the electrode during the action of the welding pulse. The color of the adhesive layer changed from red to gray on the side closest to the center of the joint, as marked by the red ellipse in Fig. 15D. This was attributed to the influence of high temperature on the properties of the adhesive layer.

Mechanical Properties and Fracture Mode of Joints

Figure 16 shows the load-displacement curves and joint energy absorption of the RSW and AE-RSW joints. Although the RSW joint had a large nugget, the joint underwent interface failure mode, resulting in a small displacement (~ 0.4 mm [0.015 in.]) (Fig. 16A). The peak load of the RSW joint was 4144.1 N, but its energy absorption was only 1.1 J, which indicated that the joint was brittle. Compared to the RSW joint, the AE-RSW joint exhibited significantly improved ductility and peak loads (up to 6071.7 N), and its energy absorption was as high as 9.9 J (Fig. 16B). Moreover, the load-displacement curve of the AE-RSW joint slowly decreased after reaching the peak load, which increased its displacement considerably.

Figure 17A shows the macroscopic fracture morphology of the RSW joint. Most of the area was white, and the small area was dark gray. Brittle fracture characteristics were observed in the dark-gray microstructure, and many microcracks were observed on the fractured surface, which were attributed to the brittle nature of the IMC layer (Fig. 17B). On the white fractured surface, pores extended radially from the center of the weld to the edge, which negatively influenced bonding strength (Fig. 17C). These pores cannot be avoided, even with optimized RSW welding parameters in this study. However, they can be minimized by using the ultrasonic-RSW technique (Ref. 8). There were a large number of shear dimples on the fractures around the pores, which were attributed to the ductile fracture of the aluminum side under the action of shear stress (Fig. 17D).

Figure 18 shows the fracture morphology of the AE-RSW joint. Interface failure of the AE-RSW joint was prevented because a weld nugget with sufficient strength was formed between the locking material and the steel. After the tensile shear test, the aluminum alloy on the loading side was separated from the weld, and the cracks propagating out-

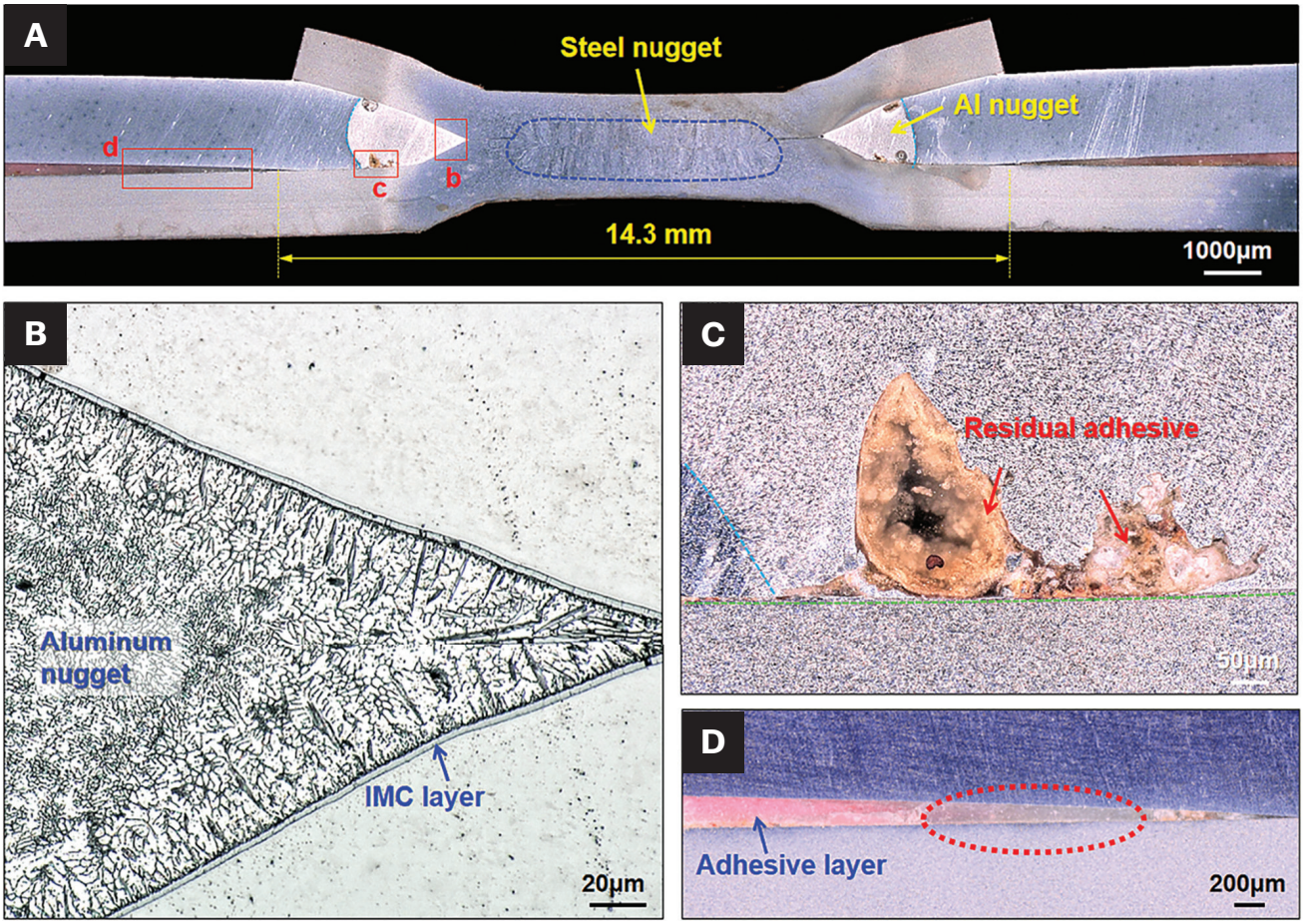

Fig. 15 — Structural characteristics of the AE-RSWB joint: A — Cross-sectional structure; B–D — enlarged views of selected region.

ward on the aluminum alloy at both sides of the weld caused complete joint fracture; meanwhile, the aluminum alloy at the nonloading side underwent severe warping deformation (Fig. 18A). There were continuous cracks in the IMC layer at the aluminum nugget-steel interface at the aluminum loading side (Fig. 18B), which were attributed to the large stress concentration at the edge of the weld. On the nonloaded side of the aluminum, the locking sheet was driven to fracture along the plate thickness direction from the nugget edge because of the severe warping of the aluminum alloy (Fig. 18C). There were many dimples in the fracture of the steel nugget, but the fracture also showed the brittle characteristics of a cleavage fracture (Fig. 18D). A large number of shear dimples appeared at the fracture near the weld surface (Fig. 18E).

Figure 19A shows the load-displacement curves of the Al-steel AB joints and the AE-RSWB joints. The average peak load and energy absorption of the AB joint were as high as 17,383.7 N and 176.1 J, respectively (Fig. 19B). Because of the strong static mechanical properties of the AB joint, the aluminum workpiece outside the lap area underwent large plastic deformation under the influence of tensile shear until the joint was completely fractured, which resulted in considerable displacement in the AB joint (Fig. 19A). As shown in Fig. 19B, there were two types of fracture morphologies of the adhesive layer in the AB joint. First, interface fracture occurred between the adhesive layer and the aluminum interface, and there were many small, flaky adhesive structures on the fracture (Fig. 19b1). The other type of fracture exhibited a discontinuous adhesive layer, and large lamellar patches of the adhesive were present on the aluminum as well as steel fracture surfaces (Fig. 19b2).

The AE-RSWB joint had a peak load of 17,198.6 N, which was similar to that of the AB joint. However, its displacement was slightly lower than that of the AB joint, which resulted in lower energy absorption of 157.5 J (Fig. 19C). The main reason for the shorter displacement of AE-RSWB was that the weld prevented full-scale fracture of the adhesive layer in the overlap area. As a result, the joint ended up breaking in only half of the lap area (Fig. 19D). The decreased energy absorption of the AE-RSW joint was also attributed to the reduced bonding area of the adhesive layer around the weld damaged by the expulsion of aluminum in some joints. Similarly, the adhesive layer was fractured under shear stress, and many flaky structures were formed on the fracture surface (Fig. 19d1). However, the aluminum alloy was necked and eventually fractured under tensile stress. As a result, there were many equiaxed dimples in the fracture (Fig. 19d2).

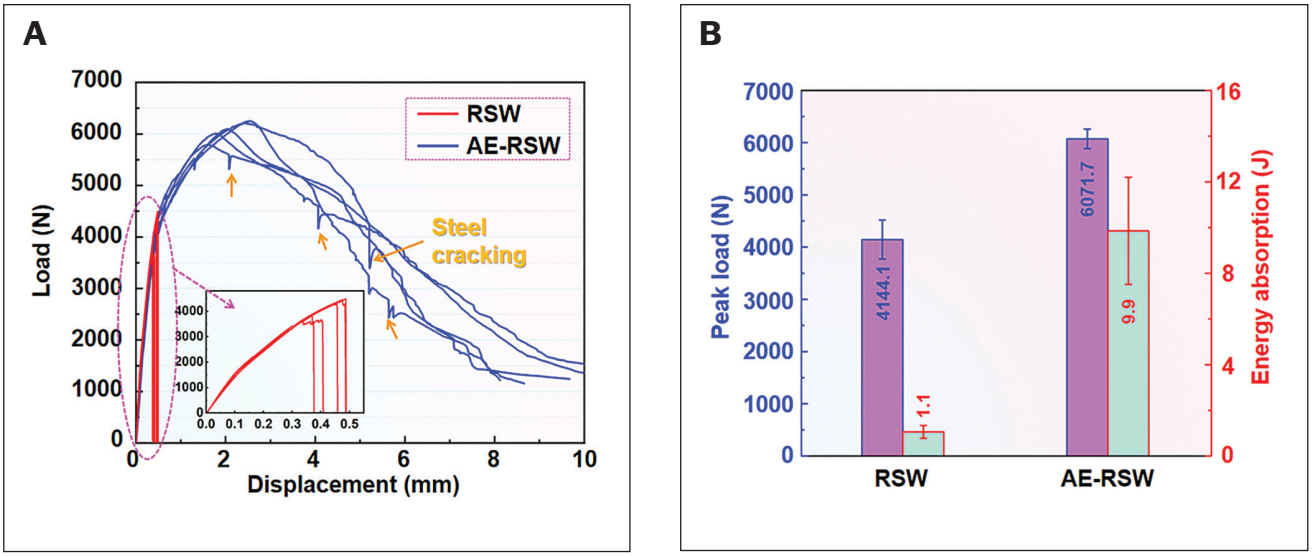

Fig. 16 — A — Load-displacement curves; B — peak load and energy absorption.

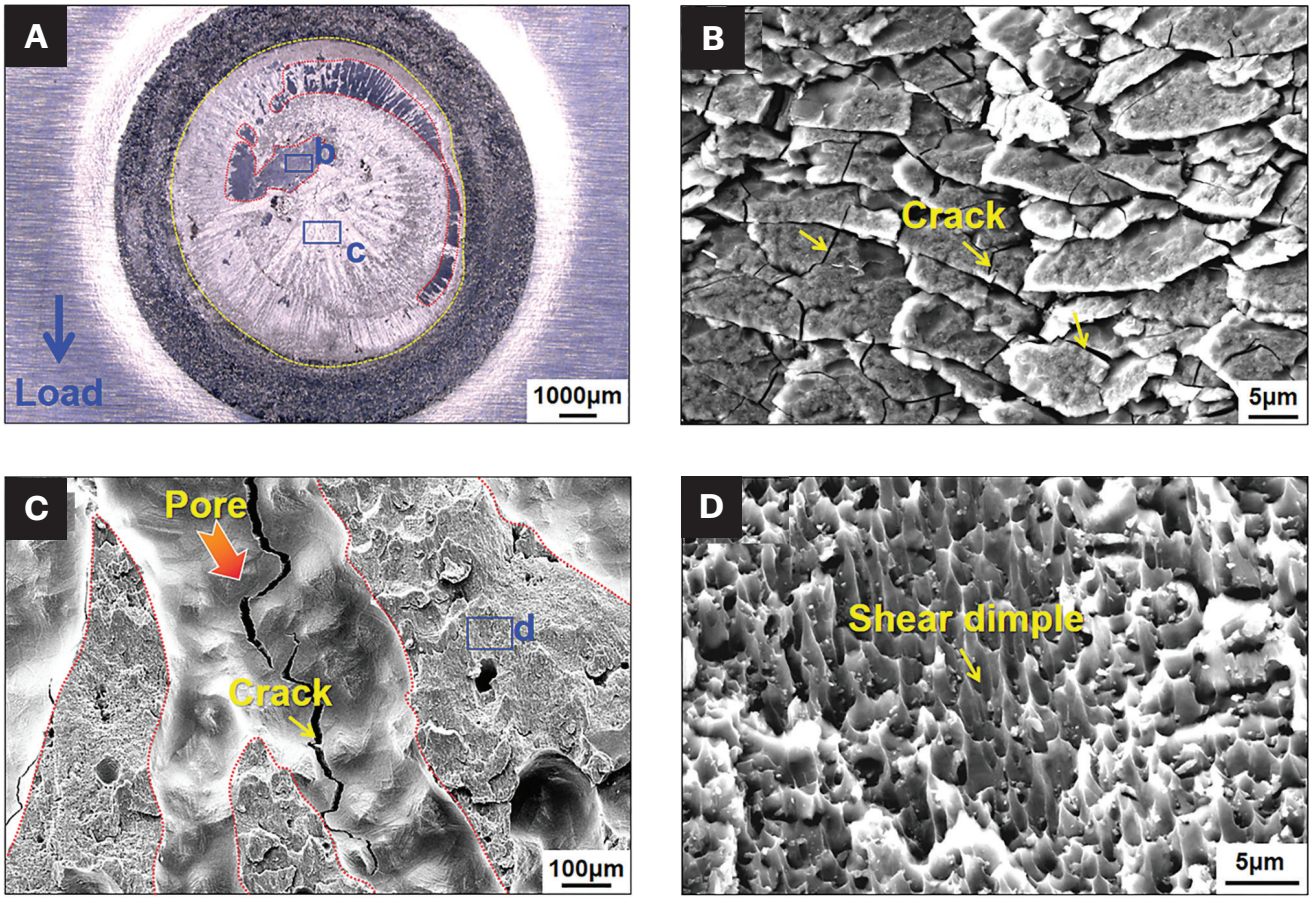

Fig. 17 — Fracture morphology of the RSW joint: A — Macromorphology of aluminum side; B–D — microstructure in the selection area.

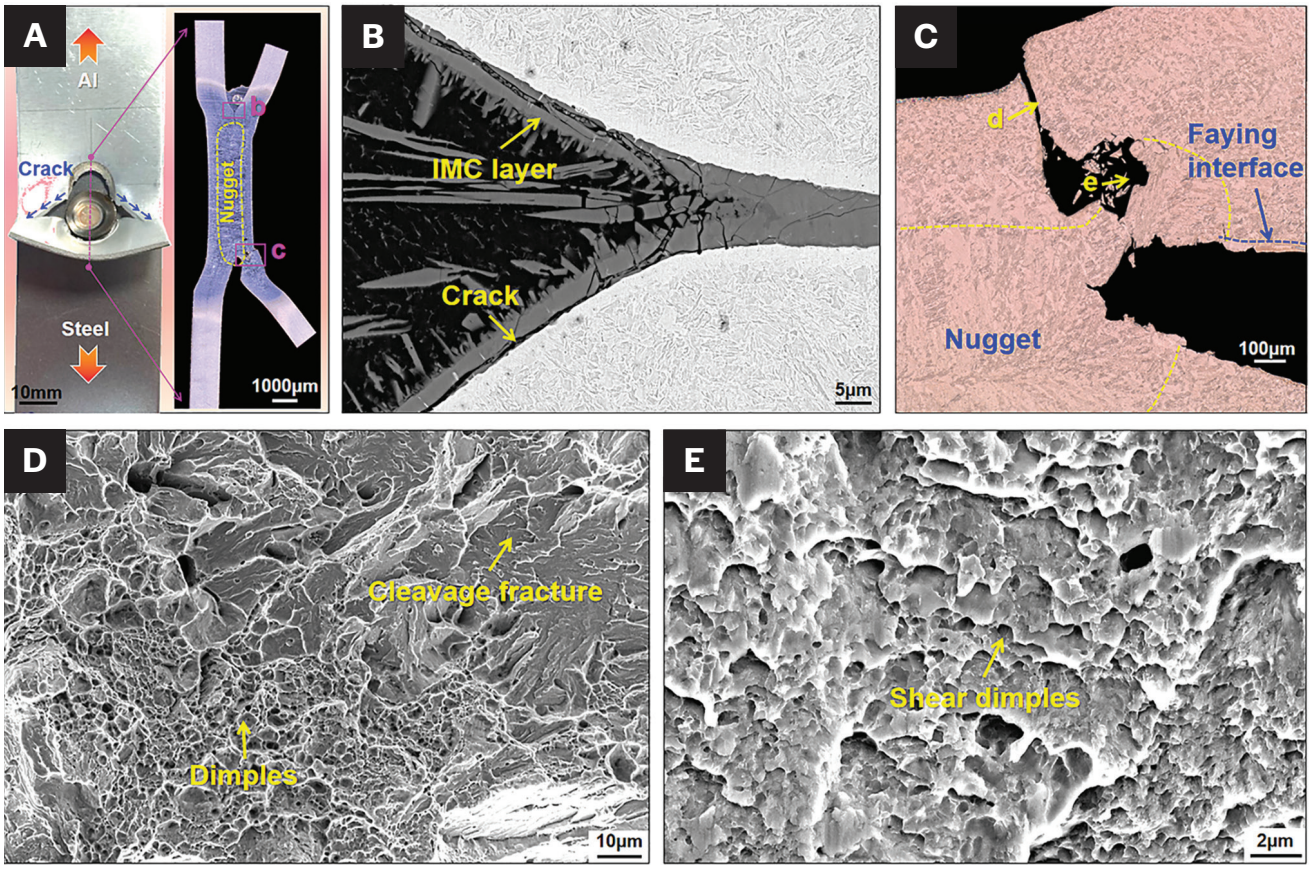

Fig. 18 — Failure modes of AE-RSW joint: A — Overall fracture morphology; B and C — enlarged view; D and E — fracture morphology at different positions marked in C.

Discussion

Control of the Expulsion Process

Expulsion in traditional RSW (such as steel-steel and Al-Al) is considered a defect that should be avoided. In particular, expulsion from the nugget usually means loss of molten metal, which decreases nugget size and hampers weld quality. The welding process used in this study actively induced expulsion of the weld, and the aluminum in the joint was completely expelled during the expulsion process in a controlled manner, thus avoiding the formation of brittle IMC that deteriorates the welding of dissimilar metals aluminum and steel. Further, this comprehensively improved the mechanical properties of the joint. The mechanism of the expulsion process is complex and influenced by several factors that vary with time, such as contact resistance, current density, resistance heat, and force generated in the weld. Therefore, it was challenging to quantitatively analyze these factors during the actual expulsion process. It was thus qualitatively evaluated using the force model proposed by Senkara (Ref. 33). The condition of expulsion was that the force (FN) from the molten nugget was greater than the force (FE) applied by the electrodes (Ref. 33). In this study, both aluminum and steel nuggets were formed in the weld, while the steel nugget was isolated inside the workpiece (Fig. 6C). Therefore, the FN was approximately derived from the liquid pressure (P) of the aluminum nugget (Fig. 20A). In addition, there was a compressive stress F_x (including F_1 and F_2) at the interface between the workpieces because of the extrusion of the electrode, which had a limiting effect on expulsion.

There are significant differences between the thermophysical properties of aluminum and steel. For example, the melting point of aluminum (~ 660°C [~ 1220°F]) is much lower than that of iron (~ 1536°C [~ 2797°F]), and the coefficient of thermal expansion of aluminum (24×10^{-6} K^{-1}) is two times greater than that of iron (11×10^{-6} K^{-1}) (Ref. 34). Based on these differences, the heat input was controlled so that expulsion only occurred for the aluminum alloy in the weld. According to Joule's law: $Q = I^2Rt$ (where Q is the total resistance heat, I is the current value, R is the total resistance, and t is the current holding time). By applying an expulsion pulse with a large current value and a short time to the joint, large resistance heat was instantly generated, which caused the aluminum alloy to melt rapidly and form high-pressure molten aluminum, which in turn caused the force (FN) to rapidly increase and reach the expulsion condition. In addition, under the combined action of heat and electrode clamping force, slight warping occurred in the peripheral area of the locking sheet, resulting in decreased contact interface with compressive stress (F_1), which was more conducive to the molten aluminum breaking through the bondage of this area and being expelled from the weld (Fig. 20B). The basic condition for the aluminum alloy to be fully expelled from the

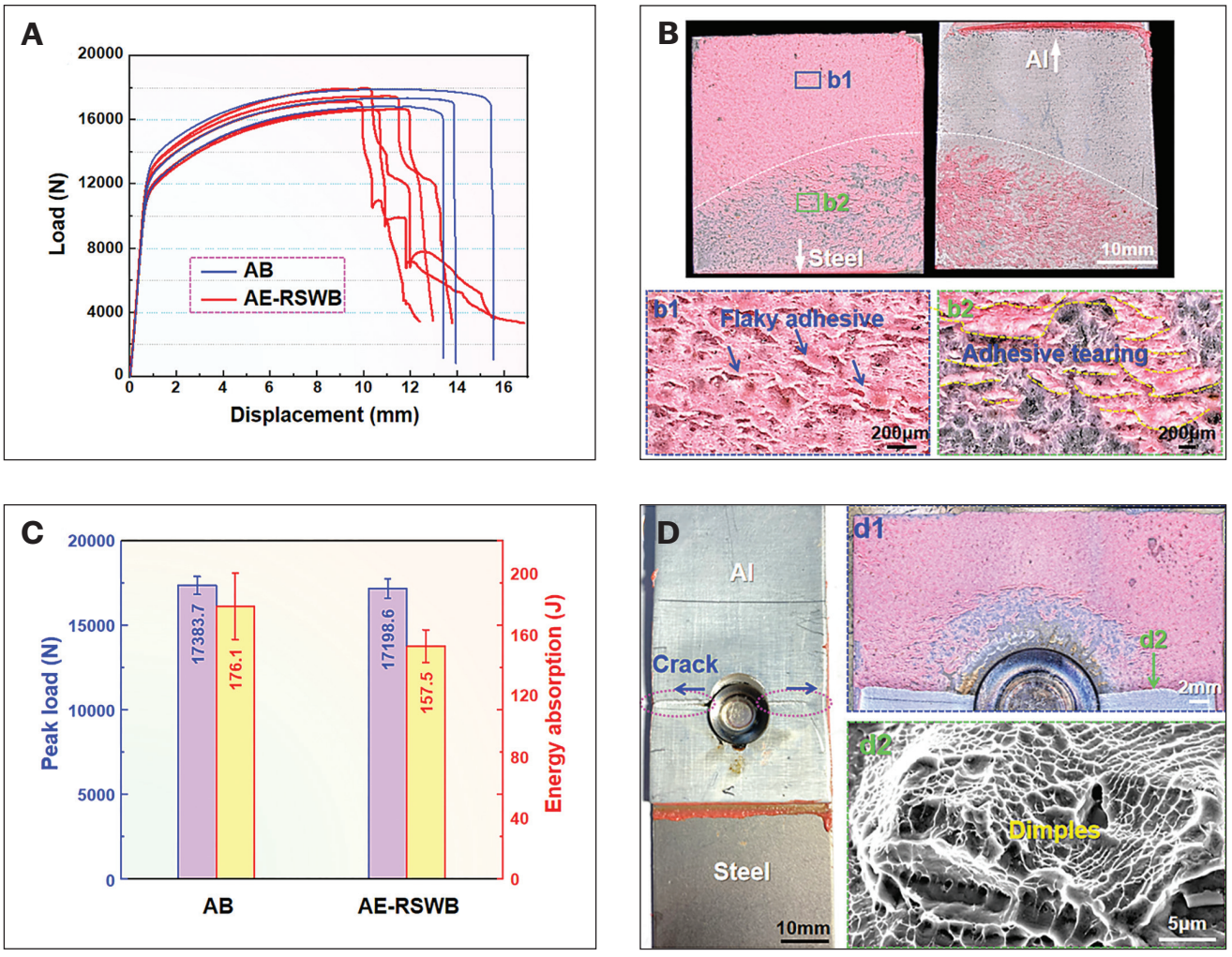

Fig. 19 — Tensile-shear performance of AB and AE-RSWB joints: A — Load-displacement curves; B — fracture morphology of AB joint; C — peak load and energy absorption; D — fracture morphology of the AE-RSWB joint.

weld was that the inner surface of the steel sheet was still in the solid state when expulsion occurred (Figs. 6B and C). Once the expulsion current was too large, excessive resistance heat promoted the steel nugget to rapidly expand to the inner surface before the expulsion of aluminum, which meant that the barrier of the solid zone between the liquid aluminum and the steel nugget was lost, causing the two liquid metals to mix and form numerous brittle phases (Fig. 6D). When there were multiple expulsion pulses, a smaller expulsion current triggered several aluminum expulsion processes, which prevented the rapid expansion of the steel nugget inside the workpiece toward the inner surface and, thus, improved the aluminum expulsion effect in the weld (Figs. 5E and H). However, the joint after the action of multiple expulsion pulses was more likely to form a common steel nugget between the locking sheet and the steel (Figs. 4 and 5H). This was because one (or two) expulsion pulses could fully remove the aluminum alloy, and the subsequent expulsion pulses promoted the interface between the locking sheet and the steel workpiece to melt and nucleate.

For the joint with the adhesive layer, the adhesive layer in the joint was pushed beyond a certain range due to the preheating effect (Fig. 8A); as a result, aluminum was completely removed during the expulsion stage to obtain a contact faying interface between the locking sheet and the steel substrate (Fig. 9A). Therefore, the adhesive layer did not significantly influence the welding process like in traditional aluminum-steel RSWB. However, the liquid pressure introduced by the adhesive layer predictably slowed the rate of engagement between the aluminum and steel workpieces (Fig. 20C). When the expulsion pulse was further applied, the melting area of aluminum was rapidly expanded, and molten aluminum had an expansion speed larger than the speed of the expelled adhesive layer in some specific direction. Under these conditions, the high-pressure molten aluminum was instantly injected into the adhesive layer in that direction (Figs. 9C and 20D).

Effect of Weld Structure on the Joint Fracture Mechanism

The aluminum alloy in the joint was completely removed by the expulsion process, creating the condition for direct welding of the locking sheet and the steel workpiece. When

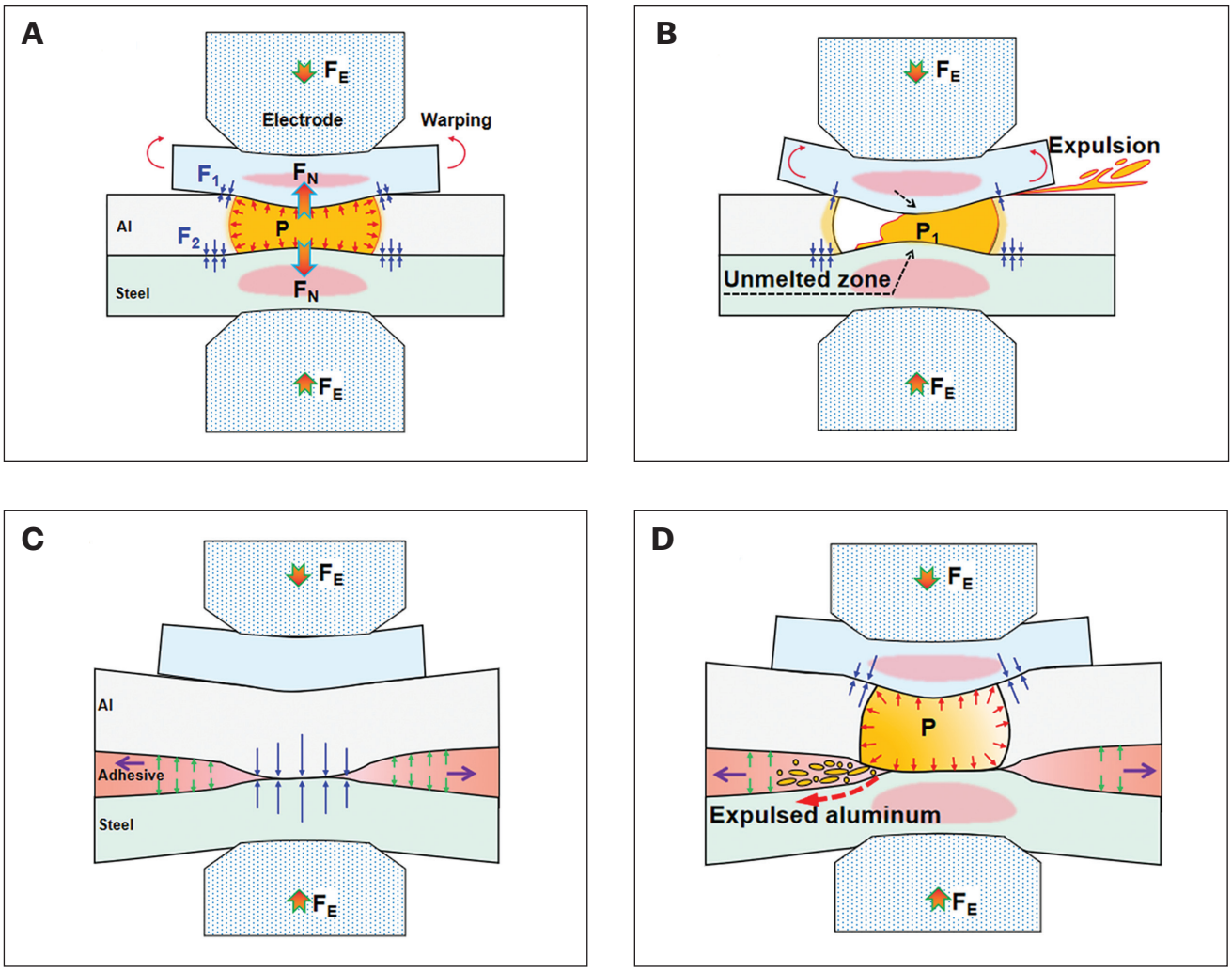

Fig. 20 — A — Forces acting on the weld during expulsion; B — expulsion process; C — preheating stage with adhesive layer; D — expulsion stage with adhesive layer

the welding pulse was applied, the faying interface between the locking sheet and the steel was heated and melted, and it formed a common steel nugget (Fig. 10B). Considering the high melting point and low thermal conductivity of steel, a smaller current and a longer welding time than the expulsion pulse were used during the welding stage, thereby ensuring that the faying interface was completely melted and a large-sized nugget was formed (Fig. 11). Because of the absence of aluminum in the joint, complete martensite was produced in the nugget under rapid cooling (Fig. 13B), which was consistent with the nugget structure of the identical steel RSW weld (Refs. 28, 31), thus ensuring excellent mechanical strength of the joint. In contrast, the absence of aluminum also allowed the joint to form a significant dent deformation, which made the periphery of the locking sheet further tightly squeezed to the joint, enhancing the clamping effect between the locking sheet and the aluminum workpiece (Fig. 10B). However, the severe dent deformation of the joint increased the contact area between the electrode tip and the weld (Fig. 21), which decreased the current density and increased the rate of heat dissipation through the electrode during welding. Accordingly, compared with the traditional RSW of Q&P1180 steel reported

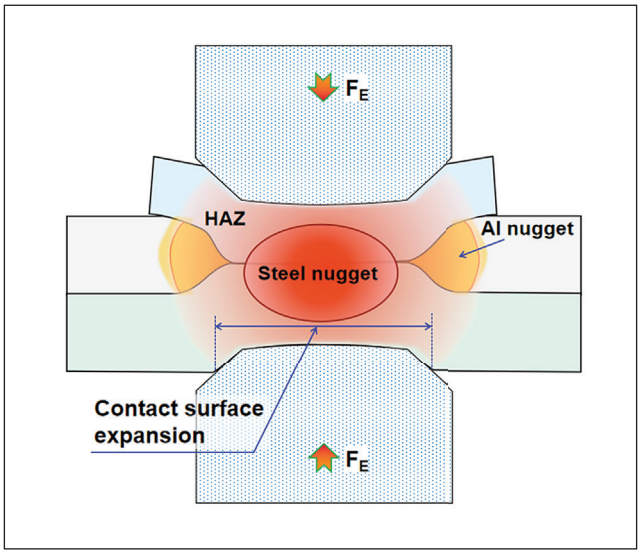

Fig. 21 — Schematic diagram of the welding process.

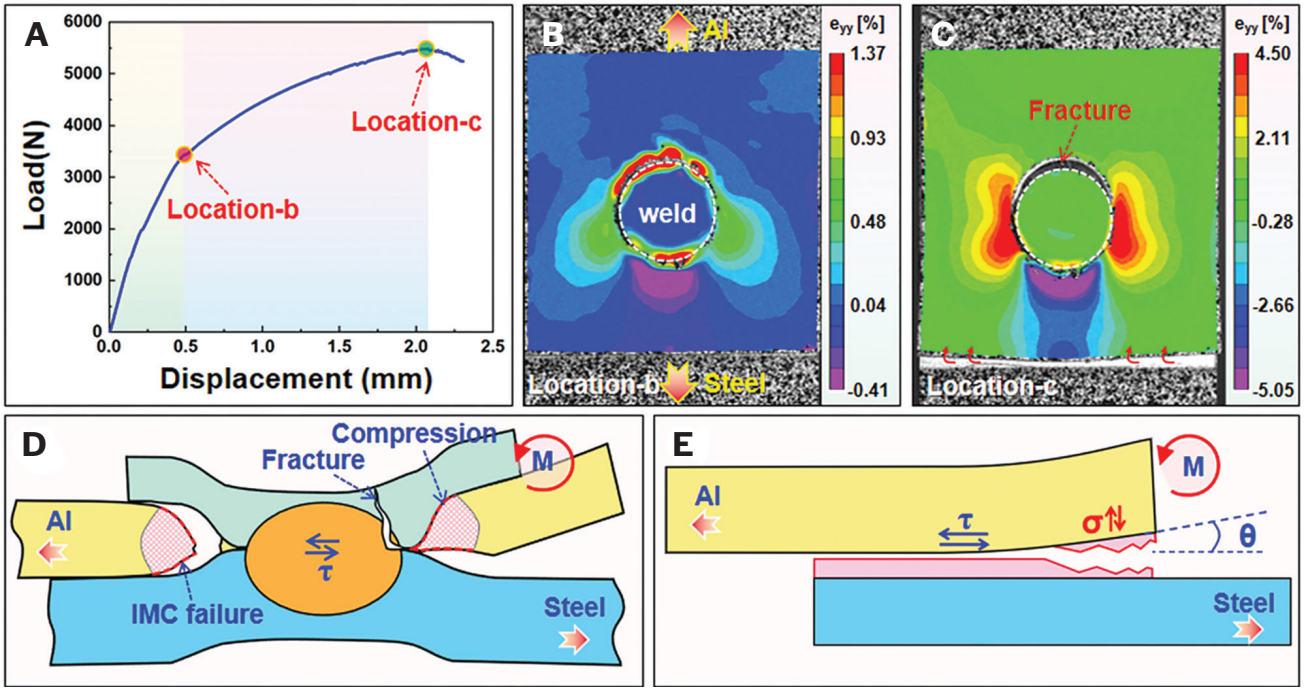

Fig. 22 — A — Load-displacement curve of the AE-RSW joint; B and C — DIC strain maps at different test stages; D and E — fracture diagrams of the AE-RSW and AB joints, respectively.

by Chen et al. (Ref. 28), the welding pulse of this study should be more than twice its welding current to promote the formation of large-sized steel nuggets. The beneficial aspect was that more resistance heat also promoted the formation of a wide HAZ around the weld, which increased the hardness and strength around the weld (Fig. 13A). In addition, the aluminum nugget around the weld further expanded during the welding stage and formed a metallurgical connection with the adjacent steel (Figs. 14A and 15B), allowing the joint to provide both mechanical and metallurgical connections.

Typically, higher hardness of a material increases its strength despite a decrease in formability (Ref. 35). The large steel nugget in the AE-RSW welds had a full martensite microstructure with high hardness, which enabled it to resist extremely strong shear stresses (τ) and avoid interface fractures like in RSW joints (Fig. 22D). When the load gradually increased to location-b during the tensile shear test, the curve approximated the change rule of elastic deformation (Fig. 22A). At this stage, the weld edge on the aluminum loading side showed a strong tensile strain distribution due to high stress concentration (Fig. 22B). As a result, the IMC layer between the aluminum nugget and the steel broke under high tensile stress (Fig. 18B). Before the load increased to location-c, the curve exhibited the characteristics of plastic deformation (Fig. 22A). The strain distribution diagram in Fig. 22B shows that aluminum was gradually separated from the upper side of the weld, and tensile strain was highly concentrated on the aluminum on both sides of the weld. This phenomenon explained why the final aluminum fracture occurred on both sides of the weld (Fig. 18A). However, the weld prevented the deformation process of the aluminum alloy on the lower side and then showed significant compressive strain on this side (Fig. 22C); as a result, the aluminum alloy gradually produced warping deformation. As the load decreased from the maximum, the warpage of aluminum on the nonloaded side increased and further enhanced the compression effect on the locking sheet, which finally led to the fracture of the locking sheet (Fig. 22D).

For AB joints shown in Fig. 22E, the adhesive layer with interface fracture was mainly driven by shear stress (τ). As the loading progresses, however, the additional bending moment (M) drives the joint to rotate. As a result, the adhesive layer on the nonloaded side fractured due to the tensile stress (σ), which resulted in discontinuous fracture of the adhesive layer (Fig. 19b2). Due to the presence of high-strength welds in AE-RSWB, the shear resistance of the joints was improved, and comprehensive interface fractures were prevented (Fig. 19D).

Advantages and Future Work of AE-RSW

AE-RSW effectively removed the light metal with a low melting point in the welding area and also enabled the flat locking sheet to achieve in situ rapid deformation and directly contact the steel workpiece to form a locking structure (Fig. 5). Furthermore, the expulsion pulse had a large adjustment range (~ 3 kA), which was conducive to the flexible design of the welding parameters and expanded the dissimilar material combination ranges, avoiding the need for a specific welding schedule for different combinations of aluminum steel. After the welding pulse was applied, a reliable joint was produced because of the formation of a locking structure between the locking sheet and the steel sheet, which tightly locked the aluminum alloy. This approach resulted in higher reliable weld strength than in the case of traditional RSW joints because in this case, brittle IMC layers were not produced in the weld nugget (Fig. 13). In addition, the unique welding schedule of AE-RSW can be easily applied using a typical RSW controller,

and it would require only regular welding cycle time and normal weld electrodes. Thus, the proposed method is beneficial for maintaining production efficiency similar to a normal RSW process. The advantages of AE-RSW are summarized below.

A) It is not necessary to predrill a hole (like in REW) before welding. AE-RSW can directly weld workpieces widely used in BIW, leading to lower cycle time and better manufacturing flexibility. It also avoids the welding problems caused by factors such as assembly errors, which can result in misalignment of the electrode axis with a predrilling hole center.

B) Compared with the rivets for REW and SPR techniques, the locking sheet has a more concise structure, which facilitates production and reduces manufacturing costs. Moreover, the locking sheet prevents poor weld quality induced by the REW rivet inclination.

C) AE-RSW is not influenced by the surface state of the workpiece, such as oxide films, coatings, and adhesive layers, which are key factors affecting weld performance and its stability for traditional RSW of aluminum to steel.

D) In AE-RSW, direct contact between the electrode and the surface of the aluminum alloy is avoided to prevent the rapid deterioration of the electrode like in traditional aluminum-steel RSW, thereby ensuring the stability of the weld and the long service life of the welding electrode.

An obvious limitation of AE-RSW is that the intentionally induced expulsion sprays into the surrounding space, which may potentially damage the component and the equipment around the weld joint. In addition, a small amount of expulsion metal may adhere to the edge of the locking sheet (Fig. 1A). This can lead to costs for painting and surface quality maintenance. Further studies are needed to overcome this shortcoming. One of our concepts is to optimize the locking sheet design, such as designating an annular cavity around the locking sheet to accommodate the expulsion metal escaping from the joint. Moreover, equipment for continuous feeding of the locking sheet is also crucial for realizing the industrial application of AE-RSW.

Conclusions

In this study, an innovative AE-RSW process was proposed to join aluminum and steel. The effect of the number and intensity of expulsion pulses on the removal of aluminum alloy and the adhesive layer from the aluminum-steel interface was systematically investigated. The microstructure characteristics, mechanical properties, and failure modes of the joints were analyzed. The main results are summarized as follows.

1) The designated expulsion process can instantly and almost completely remove molten aluminum alloy from the faying interface and clean the interface, which essentially avoids the formation of brittle compounds, resulting in improved mechanical properties of the joint. The application of three expulsion pulses was determined as optimal for efficiently removing the aluminum alloy from the interface.

2) When the adhesive layer was present at the faying interface, the expulsion pulse could also quickly remove the adhesive layer along with the molten aluminum alloy, resulting in a clean faying interface. The presence of the adhesive layer slowed the tight fitting speed of the aluminum alloy and steel workpieces; thus, it can lead to the injection of molten aluminum into the adhesive layer, thus damaging some portion of the adhesive layer.

3) A weld nugget with a large diameter was achieved by the welding pulse between the steel workpiece and the locking sheet, which strongly locked the aluminum alloy in the joint. The aluminum-steel AE-RSW joint and the AE-RSWB joint both exhibited excellent mechanical properties.

4) Thus, AE-RSW can successfully weld aluminum to steel. By optimizing the geometry, structure, and materials of the locking sheet, the proposed process can be used as a highly efficient and reliable joining solution for multiple dissimilar materials.

Declaration of Competing Interest

The authors declare that they have no known competing financial interests or personal relationships that could have appeared to influence the work reported in this paper.

Acknowledgment

This work was supported by the Science and Technology Commission of Shanghai Municipality [NO. 19XD1433500].

References

1. Cao, X. B., Zhou, X. F., Wang, H. R., Luo, Z., and Duan, J. A. 2020. Microstructures and mechanical properties of laser offset welded 5052 aluminum to press-hardened steel. *Journal of Materials Research and Technology* 9: 5378–5390. DOI: 10.1016/j.jmrt.2020.03.064

2. Qin, G. L., Ji, Y., Ma, H., and Ao, Z. Y. 2017. Effect of modified flux on MIG arc brazing-fusion welding of aluminum alloy to steel butt joint. *Journal of Materials Processing Technology* 245: 115–121. DOI: 10.1016/j.jmatprotec.2017.02.022

3. Deng, S. G., Yuan, R., Tang, X. H., and Lu, F. G. 2020. Migration behavior of IMC layer in twin-spot laser welding-brazing of aluminum to steel. *Materials & Design* 188: 108489. DOI: 10.1016/j.matdes.2020.108489

4. Hatano, R., Ogura, T., Matsuda, T., and Hirose, A. 2018. Relationship between intermetallic compound layer thickness with deviation and interfacial strength for dissimilar joints of aluminum alloy and stainless steel. *Materials Science and Engineering: A* 735: 361–366. DOI: 10.1016/j.msea.2018.08.065

5. Dong, H. G., Liao, C. Q., Yang, L. Q., and Dong, C. 2012. Effects of post-weld heat treatment on dissimilar metal joint between aluminum alloy and stainless steel. *Materials Science and Engineering: A* 550: 423–428. DOI: 10.1016/j.msea.2012.04.110

6. Hu, S. Q., Haselhuhn, A. S., Ma, Y. W., Li, Y. B., Carlson, B. E., and Lin, Z. Q. 2020. Influencing mechanism of inherent aluminum oxide film on coach peel performance of baked Al-Steel RSW. *Materials & Design* 197: 109250. DOI: 10.1016/j.matdes.2020.109250

7. Hu, Y. Y., Zhang, Y. M., Mi, G. Y., Wang, C. M., Zhang, W., and Zhang, X. 2021. Effects of Si contents in filling wires on microstructure evolution and properties of Al-steel dissimilar joint by laser welding-brazing. *Journal of Materials Research and Technology* 15: 1896–1904. DOI: 10.1016/j.jmrt.2021.09.053

8. Shah, U., and Liu, X. 2019. Effects of ultrasonic vibration on resistance spot welding of transformation induced plasticity steel 780 to aluminum alloy AA6061. *Materials & Design* 182: 108053. DOI: 10.1016/j.matdes.2019.108053

9. Yan, F., Wang, X., Chai, F., Ma, H. J., Tian, L. L., Du, X. Z., Wang, C. M., and Wang, W. 2019. Improvement of microstructure and performance for steel/Al welds produced by magnetic field assisted laser welding. *Optics & Laser Technology* 113: 164–170. DOI: 10.1016/j.optlastec.2018.12.030

10. Hu, S. Q., Haselhuhn, A. S., Ma, Y. W., Li, Z. R., Qi, L., and Li, Y. B. 2022. Effect of external magnetic field on resistance spot welding of aluminium to steel. *Science and Technology of Welding and Joining* 27: 84–91. DOI: 10.1080/13621718.2021.2013707

11. Leger, R., Roy, A., and Grandidier, J. C. 2013. A study of the impact of humid aging on the strength of industrial adhesive joints. *International Journal of Adhesion and Adhesives* 44: 66–77. DOI: 10.1016/j.ijadhadh.2013.02.001

12. Zhu, X. B., Yang, X., Li, Y. B., and Carlson, B. E. 2016. Reinforcing cross-tension strength of adhesively bonded joints using metallic solder balls. *International Journal of Adhesion and Adhesives* 68: 263–272. DOI: 10.1016/j.ijadhadh.2016.04.009

13. Zhu, X. B., Li, Y. B., Ni, J., and Lai, X. M. 2016. Curing-induced debonding and its influence on strength of adhesively bonded joints of dissimilar materials. *Journal of Manufacturing Science and Engineering* 138: 061005. DOI: 10.1115/1.4032081

14. Pouranvari, M., and Safikhani, E. 2018. Mechanical properties of martensitic stainless steel weld/adhesive hybrid bonds. *Science and Technology of Welding and Joining* 23: 227–233. DOI: 10.1080/13621718.2017.1363453

15. Chen, N. N., Wang, H. P., Wang, M., Carlson, B. E., and Sigler, D. R. 2019. Schedule and electrode design for resistance spot weld bonding Al to steels. *Journal of Materials Processing Technology* 265: 158–172. DOI: 10.1016/j.jmatprotec.2018.10.011

16. Ma, Y. W., Lou, M., Li, Y. B., and Lin, Z. Q. 2017. Effect of rivet and die on self-piercing rivetability of AA6061-T6 and mild steel CR4 of w282–294. DOI: 10.1016/j.jmatprotec.2017.08.020

17. Meschut, G., Janzen, V., and Olfermann, T. 2014. Innovative and highly productive joining technologies for multi-material lightweight car body structures. *Journal of Materials Engineering & Performance* 23: 1515–1523. DOI: 10.1007/s11665-014-0962-3

18. Shan, H., Ma, Y. W., Niu, S, Z., Yang, B. X., Lou, M., Li, Y. B., and Lin, Z. Q. 2021. Friction stir riveting (FSR) of AA6061-T6 aluminum alloy and DP600 steel. *Journal of Materials Processing Technology* 295: 117156. DOI: 10.1016/j.jmatprotec.2021.117156

19. Yu, J., Zhang, H. T., Wang, B., Cao, C., Sun, Z. C., and He, P. 2021. Dissimilar metal joining of Q235 mild steel to Ti6Al4V via resistance spot welding with Ni-Cu interlayer. *Journal of Materials Research and Technology* 15: 4086–4101. DOI: 10.1016/j.jmrt.2021.10.039

20. Sigler, D. R., Carlson, B. E., Myasnikowa, Y., and Karagoulis, M. J. 2018. Multistep direct welding of an aluminum based workpiece to a steel workpiece. U.S. Patent No. 9999938B2, filed August 20, 2014, and issued June 19, 2018.

21. Kang, J. D., Rao, H. M., Sigler, D. R., and Carlson, B. E. 2017. Tensile and fatigue behaviour of AA6022-T4 to IF steel resistance spot welds. *Procedia Structural Integrity* 5: 1425–1432. DOI: 10.1016/j.prostr.2017.07.207

22. Sun, M., Niknejad, S. T., Gao, H., Wu, L., and Zhou, Y. 2016. Mechanical properties of dissimilar resistance spot welds of aluminum to magnesium with Sn-coated steel interlayer. *Materials & Design* 91: 331–339. DOI: 10.1016/j.matdes.2015.11.121

23. Baek. S., Go, G. Y., Park, J. W., Song, J. H., Lee, H. C., Lee, S. J., Chen, C. T., Kim, M. S., and Kim, D. J. 2022. Microstructural and interface geometrical influence on the mechanical fatigue property of aluminum/high-strength steel lap joints using resistance element welding for lightweight vehicles: experimental and computational investigation. *Journal of Materials Research and Technology* 17: 658–678. DOI: 10.1016/j.jmrt.2022.01.041

24. Wang, S., Li, Y., Yang, Y., Manladan, S. M., and Luo, Z. 2021. Resistance element welding of 7075 aluminum alloy to Ti6Al4V titanium alloy. *Journal of Manufacturing Processes* 70: 300–306. DOI: 10.1016/j.jmapro.2021.08.047

25. Li, M. F., Yang, S. L., Tao, W., and Wang, Y. J. Dissimilar metal joint and resistance welding method therefore. WO2023065797A1. 2023-04-27. PCT/CN2022/113073.

26. Zhang, H., and Senkara, J. 2011. *Resistance welding: Fundamentals and applications, Second Edition. CRC Press*: Boca Raton, Fla.: CRC Press. DOI: 10.1201/b11752

27. Wang, Z. W., Liu, M., Zhang, H., Xie, G. M., Xue, P., Wu, L. H., Zhang, Z., Ni, D. R., Xiao, B. L., and Ma, Z. Y. 2022. Welding behavior of an ultrahigh-strength quenching and partitioning steel by fusion and solid-state welding methods. *Journal of Materials Research and Technology* 17: 1289–1301. DOI: 10.1016/j.jmrt.2022.01.086

28. Chen, T., Ling, Z. X., Wang, M., and Kong, L. 2021. Effect of post-weld tempering pulse on microstructure and mechanical properties of resistance spot welding of Q&P1180 steel. *Materials Science and Engineering: A* 831: 142164. DOI: 10.1016/j.msea.2021.142164

29. Chen, N. N., Wan, Z. X., Wang, H. P., Li, J. J., Solomon, J. S., and Carlson, B. E. 2020. Effect of Al-Si coating on laser spot welding of press hardened steel and process improvement with annular stirring. *Materials & Design* 195: 108986. DOI: 10.1016/j.matdes.2020.108986

30. Pouranvari, M., and Marashi, S. P. H. 2011. Failure mode transition in AHSS resistance spot welds. Part I. Controlling factors. *Materials Science and Engineering: A* 528: 8337–8343. DOI: 10.1016/j.msea.2011.08.017

31. Liu, X. D., Xu, Y. B., Misra, RDK., Peng, F., Wang, Y., and Du, Y. B. 2019. Mechanical properties in double pulse resistance spot welding of Q&P 980 steel. *Journal of Materials Processing Technology* 263: 186–197. DOI: 10.1016/j.jmatprotec.2018.08.018

32. Jiang, X. Q., Fan, X.G., Zhan, M., Wang, R., and Liang, Y. F. 2021. Microstructure dependent strain localization during primary hot working of TA15 titanium alloy: Behavior and mechanism. *Materials & Design* 203: 109589. DOI: 10.1016/j.matdes.2021.109589

33. Senkara, J., Zhang, H., and Hu, S. J. 2004. Expulsion prediction in resistance spot welding. *Welding Journal* 83(4): 123-S to 132-S.

34. Yang, J., Oliveira, J. P., Li, Y. L., Tan, C. W., Gao, C. K., Zhao, Y. X., and Yu, Z. S. 2021. Dissimilar laser techniques for joining of aluminum alloys to steels: A critical review. *Journal of Materials Processing Technology* 301: 117443. DOI: 10.1016/j.jmatprotec.2021.117443

35. Baek, S., Song, J., Lee, H. C., Park, S. Y., Song, K. H., Lee, S., Lee, S. J., Chen, C., and Kim, D. 2022. Robust bonding and microstructure behavior of aluminum/high-strength steel lap joints using resistance element welding process for lightweight vehicles: Experimental and numerical investigation. *Materials Science and Engineering: A* 833: 142378. DOI: 10.1016/j.msea.2021.142378

MINGFENG LI, **YANJUN WANG**, **WU TAO**, and **SHANGLU YANG** (*yangshanglu_lab@126.com*) are with the Shanghai Institute of Optics and Fine Mechanics, Chinese Academy of Sciences, Shanghai, China. LI is also with the University of Chinese Academy of Sciences, Beijing, China. In addition, YANG is also with the Center of Materials Science and Optoelectronics Engineering, University of Chinese Academy of Sciences, Beijing, China.